

# From Young Massive Clusters to Old Globular Clusters: Density Profile Evolution and IMBH Formation

KULDEEP SHARMA <sup>1,2</sup> AND CARL L. RODRIGUEZ <sup>2</sup>

<sup>1</sup>*McWilliams Center for Cosmology  
Carnegie Mellon University*

*5000 Forbes Ave, Pittsburgh, PA 15213, USA*

<sup>2</sup>*Department of Physics and Astronomy  
University of North Carolina at Chapel Hill*

*120 E. Cameron Ave, Chapel Hill, NC, 27599, USA*

## ABSTRACT

The surface brightness profiles of globular clusters are conventionally described with the well-known King profile. However, observations of young massive clusters (YMCs) in the local Universe suggest that they are better fit by simple models with flat central cores and simple power-law densities in their outer regions (such as the Elson-Fall-Freeman, or EFF, profile). Depending on their initial central density, these YMCs may also facilitate large numbers of stellar collisions, potentially creating very massive stars that will directly collapse to intermediate-mass black holes (IMBHs). Using Monte Carlo  $N$ -body models of YMCs, we show that EFF-profile clusters transform to Wilson or King profiles through natural dynamical evolution, but that their final  $W_0$  parameters do not strongly correlate to their initial concentrations. The most centrally-dense YMCs can produce runaway stellar mergers as massive as  $4000 M_{\odot}$  (the largest resolved mass in our simulations) which can collapse to produce IMBHs of similar masses. In doing so, these runaway collisions also deplete the clusters of their primordial massive stars, reducing the number of stellar-mass BHs by as much as  $\sim 40\%$ . This depletion will accelerate the core collapse of clusters, suggesting that the process of IMBH formation itself may produce the high densities observed in some core-collapsed clusters.

*Keywords:* Star clusters — runaway collisions — intermediate-mass black holes

## 1. INTRODUCTION

Pair-instability supernovae (PISN) and pulsational pair-instability supernovae (PPSN) suggest that it should not be possible to form black holes (BHs), through the evolution of single stars, in the mass range  $\sim 50 - 120 M_{\odot}$ , termed the “upper mass gap” (e.g., Spera & Mapelli 2017; Belczynski et al. 2016; Woosley et al. 2007). At the onset of carbon burning in an evolved star with a helium core mass in the  $45 - 135 M_{\odot}$  range, electron-positron pairs are produced (Barkat et al. 1967). The pair production depletes the energy of the star, reducing the internal radiation pressure. This reduction in internal pressure leads to a partial collapse of the core, which accelerates nuclear burning of heavy elements, culminating in a runaway thermonuclear ex-

plosion. For the stars with helium core mass in the range  $\sim 45 - 65 M_{\odot}$ , the pair-instability leads to PPSN: violent pulsations that reduce the mass and entropy of helium and other heavy elements until the pulsations damp out (e.g., Heger & Woosley 2002; Woosley et al. 2007; Woosley 2017). If the helium core mass is larger than  $65 M_{\odot}$  then the star undergoes PISN and the thermonuclear explosion completely destroys the star.

However, the gravitational wave event GW190521, resulting from the merger of two BHs of masses  $66 M_{\odot}$  and  $85 M_{\odot}$  was the first observational evidence of BHs existing in the “upper mass gap”. BHs with masses in the range of  $10^2 - 10^5 M_{\odot}$  are called intermediate-mass black holes (IMBHs, see Greene et al. 2020, for a review). The Gravitational-Wave Transient Catalog 3 (GWTC-3, The LIGO Scientific Collaboration et al. 2021b) compiled by including all the gravitational wave events from the first three observing runs of the Ad-

vanced Laser Interferometer Gravitational-Wave Observatory (LIGO, [Aasi et al. 2015](#)) and Advanced Virgo ([Acernese et al. 2014](#)), lists fifteen Binary Black Hole (BBH) merger events with at least one component mass higher than  $45 M_{\odot}$ , three events with both component masses above  $45 M_{\odot}$ , and six with at least one BH more massive than  $60 M_{\odot}$  ([The LIGO Scientific Collaboration et al. 2021a](#)). It is imperative to understand the formation scenarios of BHs with a mass in or above the mass gap.

There are several proposed mechanisms for the formation of BHs with masses  $\sim 50 - 10^5 M_{\odot}$ . Stars in the early universe (Pop III stars) were extremely metal-poor and mostly composed of hydrogen (e.g., [Madau & Rees 2001](#); [Bromm & Larson 2004](#), and references therein). The inability of molecular hydrogen to efficiently cool down would have led to Pop III stars being quite massive (see [Karlsson et al. 2013](#), for a review). The first formation scenario involves the direct collapse of these massive stars, resulting in massive BHs ([Fryer et al. 2001](#)). Unfortunately, detecting Pop III stars, whether isolated or in clusters, appears to be beyond the reach of even the James Webb Space Telescope (JWST, [Rydberg et al. 2013](#)). Second, gravitational instabilities during the inflationary era could have formed BHs of  $\sim 1 - 10^3 M_{\odot}$  ([Carr et al. 2016](#)), and BHs of  $\sim 10^3 - 10^5 M_{\odot}$  in the early universe from collapsing gas clouds without going through all the stages of stellar evolution (e.g., [Loeb & Rasio 1994](#); [Bromm & Loeb 2003](#)). These BHs can serve as seeds for the supermassive BHs seen at the centers of present-day galaxies. Third, gravitational runaway mergers in high-density central environments of star clusters can produce BHs of mass  $10^2 - 10^4 M_{\odot}$ . Gravitational runaways can be divided into two categories based on timescale. The slow scenario, unfolding over a timescale of 100 Myr to a Gyr, involves hierarchical mergers of smaller BHs, and can produce IMBHs of mass  $10^2 - 10^3 M_{\odot}$  (e.g., [Miller & Hamilton 2002](#); [McKernan et al. 2012](#); [Rodriguez et al. 2018, 2019](#); [Fragione & Silk 2020](#); [Fragione et al. 2020, 2022](#); [Rizzuto et al. 2022](#)).

The fast scenario involves collisional runaway mergers of massive stars in dense star clusters and unfolds on a short timescale of tens of Myrs early in the cluster’s lifetime ([Portegies Zwart & McMillan 2002](#)). A star can collide and merge with another star, grow its mass and physical size, and then go on to merge with other stars repeatedly in a runaway fashion. The resultant product star can become very massive, may not undergo PISN, and can collapse to form either mass gap BHs or IMBHs (e.g., [Portegies Zwart et al. 2004](#); [Di Carlo et al. 2019](#); [Banerjee et al. 2020](#); [Kremer et al. 2020b](#); [Banerjee 2021](#);

[Di Carlo et al. 2021](#); [Rizzuto et al. 2022](#); [Ballone et al. 2022](#)).

Observational evidence suggests that the majority of stars form in clustered environments, particularly so for massive stars ([Liu et al. 2021](#); [Portegies Zwart et al. 2010](#), and references therein). Given that massive stars play a crucial role in the collisional runaway mechanism of IMBH formation, it is natural to investigate the dynamical evolution of star clusters to understand collisional runaways. Various types of star clusters exist, including globular clusters (GCs), open clusters, nuclear star clusters, and young massive clusters (YMCs). YMCs typically have a mass  $> 10^4 M_{\odot}$  and age  $< 100$  Myr ([Portegies Zwart et al. 2010](#)), and it is particularly interesting to study their evolution for two reasons. Firstly, they are considered the most common birthplaces of massive stars, characterized by high central densities and young dynamical states, making them ideal candidates for the stellar collisional runaway channel of IMBH formation ([Portegies Zwart et al. 2004](#)). Secondly, YMCs are believed to be progenitors of present-day GCs ([Kruijssen 2012](#)). By studying the evolution of YMCs, we can gain insights into the processes that lead to the formation of GCs and their subsequent dynamical evolution over cosmic timescales.

[Kremer et al. \(2020b\)](#) explored the high-mass star cluster regime ( $10^5 - 10^6 M_{\odot}$ ), which is representative of the Milky-Way GC population ([Harris 1996](#)), using a suite of 68 clusters with an initial [King \(1966\)](#) density profile simulated using `Cluster Monte Carlo (CMC)` code. They found that approximately 20% of all BH progenitors undergo at least one stellar collision prior to collapse and about 1% of all BHs reside in the upper mass gap. Many of the BBHs produce second-generation BHs through mergers within the cluster. [González et al. \(2021\)](#) investigated the effect of the binary fraction of stars more massive than  $15 M_{\odot}$  on the formation of IMBHs in YMCs. Their suite of simulations, with a fixed initial cluster mass of  $4.7 \times 10^5 M_{\odot}$ , metallicity of  $0.1 Z_{\odot}$  and a King density profile, demonstrated that YMCs with larger high-mass binary fractions are more efficient in forming IMBHs.

[González et al. \(2021\)](#) used a King profile for their YMCs. However, observations strongly suggest that YMCs have extended outer halos and their surface brightness profiles are often better fitted with Elson-Fall-Freeman (EFF) profiles (e.g., [Elson et al. 1987](#); [Larsen 1999](#); [Mackey & Gilmore 2003](#); [McLaughlin & van der Marel 2005](#); [Bastian et al. 2013](#)) than with King profiles. At fixed virial radii, EFF profile clusters can have high central densities, making them dynamically more active and fertile for collisional runaways.

In this paper, we study the effect of high-mass binary fraction, initial cluster size, cluster mass, and giant star collision prescription on the short-term evolution of YMCs with an initial EFF profile. We discuss the evolution of the cluster profile from an EFF to a King profile and emphasize the formation of IMBHs through stellar runaway collisions. This paper is organized as follows: In Section 2, we provide a brief discussion of the CMC code and detail the initial conditions for cluster simulations. Section 3 outlines the fitting procedure for various density profiles to the cluster surface brightness. In Section 4, we discuss the evolution of the cluster density profile using the data from simulations. Section 5 describes important modifications made to the CMC code to handle massive star collisions and presents results from the simulation grid used to study IMBH formation through stellar collisional runaways. Finally, we summarize our findings and discuss future prospects in Section 6.

## 2. CLUSTER SIMULATIONS

We use the Hénon style Monte Carlo code CMC to simulate the evolution of star clusters. CMC includes up-to-date prescriptions for mass loss rate of massive stars, compact object formation, strong 3 and 4 body encounters using `fewbody`, gravitational-wave emission, and stellar/binary evolution prescriptions with the population synthesis code `COSMIC` (Breivik et al. 2020). We use the delayed compact object formation prescription of Fryer et al. (2012). Please refer to sections 2 and 3 of Rodriguez et al. (2022) for a discussion on various prescriptions for solving dynamical interactions within a star cluster and an overview of CMC package.

Elson et al. (1987) found that the surface brightness profiles of young star clusters are better modeled by power law fits compared to King profiles which are used to fit old evolved GCs in the MW. In EFF profiles, the 2D surface density profile is given by -

$$\mu(r) = \mu_0 \left(1 + \frac{R^2}{a^2}\right)^{-\frac{\gamma}{2}} \quad (1)$$

where  $\mu_0$  is the maximum (i.e. central) surface density, and  $R$  is the projected distance from the center of the cluster. The corresponding three-dimensional mass density  $\rho(r)$  at a radius  $r$  is given by -

$$\rho(r) = \rho_0 \left(1 + \frac{r^2}{a^2}\right)^{-\frac{\gamma+1}{2}} \quad (2)$$

where  $\rho_0$  is the mass density at the center of the cluster,  $a$  is the scale radius, and  $\gamma$  is the power law slope of the profile.

The left panel of Figure 1 shows the distribution of the EFF profile slopes for young and old star clusters, as reported in the literature. Approximately 92% of young star clusters have an EFF profile slope between 2.0 and 6.0 with a median of 2.4. It is noteworthy that the distribution of EFF profile slopes differs between the older GC populations observed in M33 and the Milky Way compared to the profiles of young star clusters.

We create two separate grids of simulations with realistic stellar evolution and a metallicity of 0.002 (equivalent to  $0.1 Z_{\odot}$  assuming a solar metallicity of 0.02). The first grid (`grid1`) of simulations is to study the evolution of the star cluster density profile from the EFF profile to an evolved GC profile like those in the MW. The second grid (`grid2`) is to study the effect of various physical parameters and initial conditions on runaway collisions and massive BH formation. In both grids the masses of single stars and primary stars (within a binary) are sampled from Kroupa (2001) initial mass function in the mass range of  $0.08 - 150 M_{\odot}$ .

`grid1` consists of initial conditions with EFF profile slopes  $\gamma \in \{2.3, 3.0, 4.0, 6.0\}$  to capture the 92% of the range of  $\gamma$  for young clusters. These clusters have cluster tidal radii,  $r_{t,0} \in \{5, 10, 20, 50, 100\}$  pc, and initial virial radii,  $r_v \in \{1, 4\}$  pc. For a cluster with mass  $M_C$  embedded in a galaxy with mass  $M_G$  at a distance of  $R_G$ , the tidal radius  $r_{t,0}$  is given as

$$r_{t,0} = \left(\frac{M_C}{3M_G}\right)^{1/3} R_G \quad (3)$$

All clusters have an initial cluster mass of  $M_{\text{cluster}} \simeq 3 \times 10^5 M_{\odot}$  corresponding to  $N = 5 \times 10^5$  stars and binaries, and a 10% initial binary fraction. This grid uses the default prescriptions in CMC for dynamics and stellar evolution.

`grid2` consists of initial conditions with EFF profile slopes  $\gamma \in \{2.3, 3.0, 4.0, 6.0\}$ ; initial cluster mass of  $M_{\text{cluster}} \simeq 6 \times 10^5 M_{\odot}$  and  $M_{\text{cluster}} \simeq 3 \times 10^5 M_{\odot}$  corresponding to  $N = 10^6$  and  $N = 5 \times 10^5$  stars and binaries, respectively; initial virial radii,  $r_v \in \{1, 4\}$  pc; and initial binary fraction for high-mass binaries ( $M > 15 M_{\odot}$ ) of 5% and 100%. Binary fraction for all the stars less massive than  $15 M_{\odot}$  is kept 5% in all the simulations. Each of these combinations is repeated for three different realizations (using different random number seeds) for two different prescriptions for stellar collisions involving giant stars (discussed below). This results in 288 star-cluster simulations. Each simulated cluster experiences a tidal force corresponding to being on a 8 kpc circular orbit inside the Milky Way.

The collision process of two main-sequence (MS) stars is modeled using the “sticky-sphere” approximation,

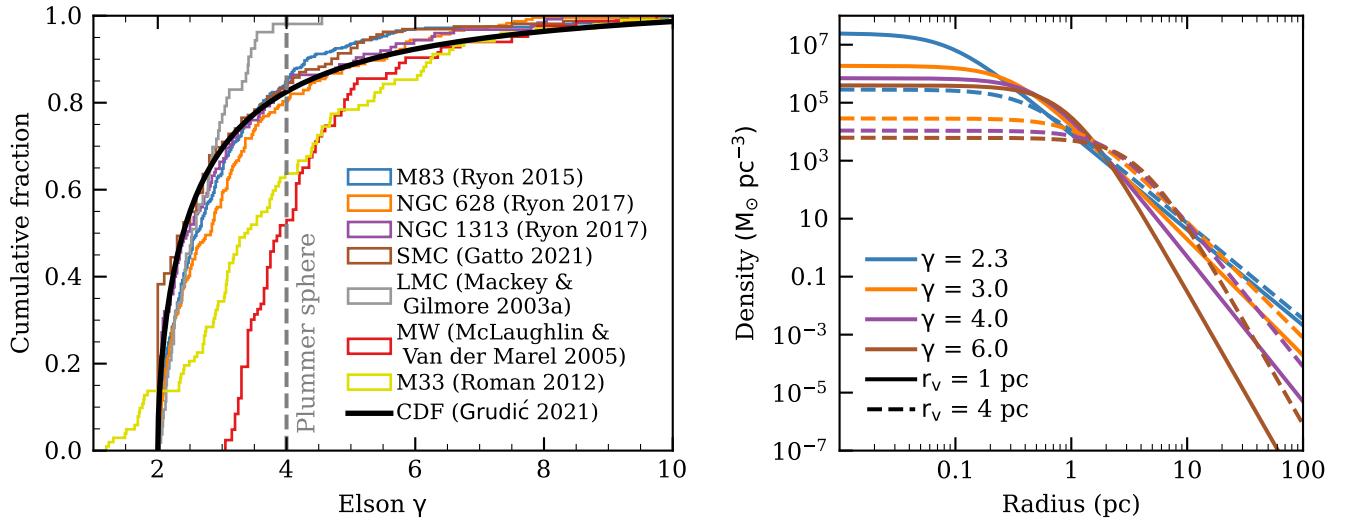


**Figure 1.** *Left panel* : shows observational data for EFF profile slopes of star clusters from the literature, along with suggested universal CDF of EFF slopes from (Grudić et al. 2021). fitted using the observational data of young star clusters in the age range  $10^6 - 10^8$  yr. The histograms show the EFF profile slopes from the observed surface brightness of star clusters in M83 (age  $< 3 \times 10^6$  yr) from Ryon et al. (2015), NGC 628 and NGC 1313 (age  $< 2 \times 10^6$  yr) from Ryon et al. (2017), M33 (age :  $10^7 - 10^9$  yr) from San Roman et al. (2012), the Large Magellanic Cloud (age :  $10^6 - 10^{10}$  yr) from Mackey & Gilmore (2003), the Small Magellanic Cloud (age :  $10^6 - 10^{10}$  yr) from Gatto et al. (2021), and the MW (age  $> 7 \times 10^9$  yr) from McLaughlin & van der Marel (2005). The CDF curve agrees well with the histograms of young star clusters. This figure is largely a reproduction of figure 2 of Grudić et al. (2018) with additional data for M33 and MW clusters. *Right panel* : shows the density of EFF profiles with different Elson  $\gamma$  and virial radii. For a fixed virial radius of the cluster, the central density  $\rho_0$  increases as Elson  $\gamma$  decreases. Furthermore, for a given Elson  $\gamma$  the central density  $\rho_0$  decreases as the virial radius of the cluster increases. Therefore, star clusters with small Elson  $\gamma$  and small virial radius are the most centrally dense and likely to facilitate IMBH formation through runaway stellar collisions.

where no mass is lost during the collision, and the mass of the merger product is the sum of the masses of the colliding stars. In a collision of two MS stars of masses  $M_1$  and  $M_2$ , the stellar age of the new product MS star is given by

$$t_3 = f_{\text{rejuv}} \frac{t_{\text{MS3}}}{M_3} \left( \frac{M_1 t_1}{t_{\text{MS1}}} + \frac{M_2 t_2}{t_{\text{MS2}}} \right) \quad (4)$$

where  $t_{\text{MS1}}$ ,  $t_{\text{MS2}}$ , and  $t_{\text{MS3}}$  are the MS lifetimes of the colliding stars and the collision product, respectively. The mass of the merger product is  $M_3 = M_1 + M_2$ ;  $t_1$  and  $t_2$  are the stellar ages of the colliding MS stars at the time of collision. The factor  $f_{\text{rejuv}}$  determines the amount of rejuvenation in the collision product through mixing of material of the colliding stars. We use the default value of  $f_{\text{rejuv}} = 1$  as suggested by Breivik et al. (2020).

However, when at least one of the colliding stars is a giant the outcome is less clear. In COSMIC the merger is treated as a common-envelope evolution, where the cores of the stars orbit within the loosely bound common envelope. Common envelope evolution is modeled through the standard  $\alpha\lambda$  prescription (see §3.2 of Breivik et al. 2020) where  $\lambda$  is a factor that determines the binding

energy of the envelope to its stellar core, while  $\alpha$  is the efficiency factor for injecting orbital energy into the envelope. We use a value of  $\alpha = 1$  and a variable  $\lambda$  that depends on the evolutionary state of the star. We adopt two different prescriptions for the collisions involving a giant star: 1) we make one attempt to merge the stars through common envelope prescription. If the stars do not merge in the first attempt, then we force them to merge (referred to as CE2, hereafter). This is the default behavior of CMC for such collisions. In this scenario some or all of the envelope of the giant star is lost. 2) stars are forced to merge in the first attempt itself (referred to as CE0, hereafter). For the merger product, the total mass is again computed as  $M_3 = M_1 + M_2$  and the core mass is computed as  $M_{c,3} = M_{c,1} + M_{c,2}$ , where  $M_{c,1}$  and  $M_{c,2}$  are the core masses of the colliding stars. This scenario mimics a sticky sphere collision.

By default in CMC the collision of a MS star or giant and a BH results in complete disruption of the star. While this prescription is reasonable for near-equal mass encounters, it likely overpredicts the disruption of massive stars and giants by small stellar-mass BHs (where at most collision speeds encountered in GCs, the BH would

pass through the envelope of a giant with minimal disruption). To that end, we modify CMC such that whenever a compact object with mass  $M_{\text{comp}}$  collides with a giant star with mass  $M_* > 100 M_{\odot}$  and  $M_{\text{comp}} < M_*/2$ , both colliding objects remain unaffected.

### 3. FITTING THE SURFACE BRIGHTNESS PROFILES

It is challenging to determine the three-dimensional positions of stars in clusters through observations without accurate distance information for individual stars. Therefore, it is common for observers to fit projected 2D profiles of theoretical models to the binned surface brightness data of star clusters.

Our simulations incorporate realistic stellar evolution, providing luminosities and effective temperatures for stars at each snapshot. We use `cmctoolkit` (Rui et al. 2021) to generate the V-band surface brightness profile of star clusters at each snapshot. `cmctoolkit` uses the individual stellar luminosities and statistical orbit averaging to generate the surface brightness profiles from a given snapshot.

We fit theoretical profiles to the generated surface brightness profile at each snapshot for the clusters in `grid1`. First, we project the 3D density  $\rho(r)$  of the theoretical model onto a two-dimensional plane by integrating along the line of sight (e.g., Binney & Tremaine 2008)

$$\Sigma(R) = 2 \int_R^{\infty} \rho(r) * \frac{r}{\sqrt{(r^2 - R^2)}} dr \quad (5)$$

Here,  $R$  is the projected radial distance from the cluster center. Assuming that light follows mass for stars (as out theoretical models are single-mass models), we can write the surface brightness as

$$\mu(R) = \mu_0 - 2.5 \log_{10}(\Sigma(R)) \quad (6)$$

At each snapshot, we fit the density profiles of King (1966), Wilson (1975), and EFF (Elson et al. 1987) models to the surface brightness profile of star clusters. For each of these isotropic density models, we use  $\chi^2$  minimization to find the best-fit parameters at each snapshot, and to compare the relative goodness of fits between the 3 model families.

The King (1966) distribution function is a single-mass lowered isothermal distribution function with a finite size defined by

$$f(\mathcal{E}) = \begin{cases} \rho_1 (2\pi\sigma^2)^{-3/2} (e^{\mathcal{E}/\sigma^2} - 1) & \mathcal{E} > 0 \\ 0 & \mathcal{E} \leq 0 \end{cases} \quad (7)$$

Here,  $\mathcal{E} = -\Phi - \frac{1}{2}v^2$  represents the relative energy of a star with velocity  $v$  in a cluster with potential  $\Phi$ . At the

tidal boundary of the system,  $\mathcal{E}$  goes to 0. The parameters  $\rho_1$  and  $\sigma$  are normalization factors, with  $\sigma$  not to be confused with the actual velocity dispersion of stars in the cluster. It represents a theoretical parameter that only coincides with the velocity dispersion in any given direction under the idealized assumption of an infinite tidal boundary.

The King model does not have an analytic expression for a density profile, and we have to numerically integrate an ODE to find the density and enclosed mass at a given radial position. A dimensionless central potential,  $W_0 = \sqrt{\frac{-\Phi(0)}{\sigma^2}}$ , uniquely sets the density profile of the system. We can find the unnormalised density,  $\rho(r)/\rho_1$ , for a given King model defined by the parameter  $W_0$ . The physical size of the system is determined by the King radius  $r_0 = \frac{9\sigma^2}{4\pi G\rho_0}$ , where  $\rho_0$  is the central mass density, and  $G$  is the gravitational constant. Using  $\rho(r)$ , we can find the surface brightness profile of a cluster with a given  $W_0$  using equations 5 and 6. We used flat priors for  $W_0$  in the range [0.1, 14] while fitting the surface brightness profiles due to numerical problems for  $W_0 < 0.1$ . For this reason, most of the disrupted clusters have  $W_0 \sim 0.1$  in Table 1.

The Wilson profile fits the GC surface brightness data better than (or equally as well as) the king models, as reported by McLaughlin & van der Marel (2005). The single-mass model distribution function for the Wilson profile is given by

$$f(\mathcal{E}) = \begin{cases} \rho_1 (2\pi\sigma^2)^{-3/2} (e^{\mathcal{E}/\sigma^2} - 1 - \mathcal{E}/\sigma^2) & \mathcal{E} > 0 \\ 0 & \mathcal{E} \leq 0 \end{cases} \quad (8)$$

Similar to the King model, the parameter  $W_0$  sets the surface brightness profile of the system and the King radius ( $r_0$ ) sets the scale of the system.

As evident from equation 1, for the EFF model, the power law exponent ( $\gamma$ ) sets the surface brightness profile of the system, while the scale radius ( $a$ ) determines the physical size.

Star clusters experience the loss of constituent bodies due to stellar evolution-induced mass loss and dynamical evolution (Lamers et al. 2010). Stellar evolution results in the ejection of compact objects if they acquire a sufficient kick velocity at birth. The dynamical evolution of a stellar system can result in the ejection of objects through various mechanisms, such as strong encounters between two or more bodies, kicks from tidal disruption events (TDEs) or GW-driven mergers, two-body relaxation, and tidal stripping of stars from a cluster embedded in a tidal field (see section 2 of Weatherford et al. 2023, and references therein for a discussion of these

**Table 1.** Relevant parameters for profile transition in simulations with  $N = 5 \times 10^5$  objects.

$\gamma$	$r_{t,0}$ (pc)	$t_{\text{disrupt}}$ Myr	$t_{\text{trans}}(T_{1/2})$		King $W_0$	$\gamma$	$r_{t,0}$ (pc)	$t_{\text{disrupt}}$ Myr	$t_{\text{trans}}(T_{1/2})$		King $W_0$
			Wilson	King					Wilson	King	
$r_v = 1 \text{ pc}$						$r_v = 4 \text{ pc}$					
2.3	5.0	90	–	0.0088	0.25	2.3	5.0	916	–	0.0088	0.1
2.3	10.0	691	–	0.0879	3.66	2.3	10.0	7532	–	0.0879	2.55
2.3	20.0	3704	0.0879	0.1757	(6.82) 9.73	2.3	20.0	> 13800	0.0879	0.3514	5.61
2.3	50.0	> 13800	0.0879	7.4677	(8.05) 10.86	2.3	50.0	> 13800	0.0879	5.1834	7.21
2.3	100.0	> 13800	0.0879	76.4331	(8.80) 9.56	2.3	100.0	> 13800	0.0878	–	–
3.0	5.0	76	–	0.0118	0.1	3.0	5.0	758	–	0.0119	0.11
3.0	10.0	616	0.1184	0.2367	0.54	3.0	10.0	6572	–	0.2367	0.13
3.0	20.0	5119	0.1184	3.5512	(5.96) 8.21	3.0	20.0	> 13800	0.1184	1.0654	4.90
3.0	50.0	> 13800	0.2367	42.0229	(7.26) 8.66	3.0	50.0	> 13800	0.1184	–	7.41
3.0	100.0	> 13800	8.8780	–	–	3.0	100.0	> 13800	2.2491	–	–
4.0	5.0	73	–	0.0108	0.10	4.0	5.0	554	–	0.0108	0.11
4.0	10.0	598	0.1075	0.3226	0.18	4.0	10.0	5289	0.1078	0.6452	0.1
4.0	20.0	4565	0.2151	6.0222	(3.74) 4.29	4.0	20.0	503	0.1077	–	–
4.0	50.0	> 13800	6.4525	53.7702	(7.69) 7.88	4.0	50.0	> 13800	0.9679	–	–
4.0	100.0	> 13800	13.4426	–	–	4.0	100.0	> 13800	–	–	–
6.0	5.0	71	0.0010	0.0500	0.10	6.0	5.0	479	–	0.0200	0.1
6.0	10.0	630	0.0993	0.8923	0.10	6.0	10.0	5667	0.0993	1.6856	0.16
6.0	20.0	5919	0.8923	5.9490	(6.45) 9.70	6.0	20.0	5038	0.5949	–	–
6.0	50.0	> 13800	8.9235	57.0111	(7.77) 8.68	6.0	50.0	> 13800	8.9235	–	–
6.0	100.0	> 13800	16.3597	–	–	6.0	100.0	> 13800	–	–	–

NOTE—The left and right halves of the table are for cluster simulations with initial virial radii of 1 pc and 4 pc, respectively. Each half has 6 columns: columns (1-2) are the initial EFF profile slope ( $\gamma$ ) and tidal radius ( $r_{t,0}$ ) of the cluster, and column 3 is the disruption time ( $t_{\text{disrupt}}$ ) of the cluster in Myr. Columns (4-5) show the transition time ( $t_{\text{trans}}$ ) for EFF  $\rightarrow$  Wilson and EFF  $\rightarrow$  King, respectively.  $t_{\text{trans}}$  is reported in units of the initial half-mass relaxation time ( $T_{1/2}$ ) of the cluster. There are four possible scenarios for the values in columns (4-5): (–, –) means that the cluster does not transition to either Wilson or King profiles and remains an EFF profile, ( $t$ , –) shows that the cluster transitions to a Wilson profile at time  $t$  and remains a Wilson cluster thereafter. (–,  $t$ ) represents a cluster which transitions to a King profile at time  $t$  without transitioning to a Wilson profile. ( $t_0, t_1$ ) shows a typical cluster that first transitions to a Wilson profile at time  $t_0$  and then to a King profile at time  $t_1$ . Finally, column 6 shows the King parameter  $W_0$  for the cluster of the best-fit model at the end of the simulation is King. If a cluster does not transition to a King-profile then column 6 is left empty. Some clusters undergo a core collapse and the value of  $W_0$  given in bracket is right before the core collapse for such models. Tidally disrupted clusters have  $W_0 \sim 0.1$ .

mechanisms). The clusters in grid1 are simulated up to the current age of the universe (13.8 Gyr). These clusters lose a significant number of objects through the tidal boundary during the evolution, and our highly tidally truncated clusters do not survive until the present age of the universe. We consider a cluster to be tidally disrupted when its mass drops below  $15000 M_\odot$  (5% of its initial mass of  $5 \times 10^5 M_\odot$ ). We do not fit density models to a cluster beyond its disruption time ( $t_{\text{disrupt}}$ ).

The fit parameters for the King and Wilson models are  $W_0$  and  $r_0$ , while for the EFF model they are  $\gamma$  and  $a$ . For a cluster at each snapshot, we fit all the three models to the surface brightness profile data and record the best-fit  $\chi^2$  values for each model. Whichever model has the lowest  $\chi^2$  is considered as the best descriptor of the cluster at that particular epoch. We also record the best-fit values of the model parameters for all the three models at these epochs.

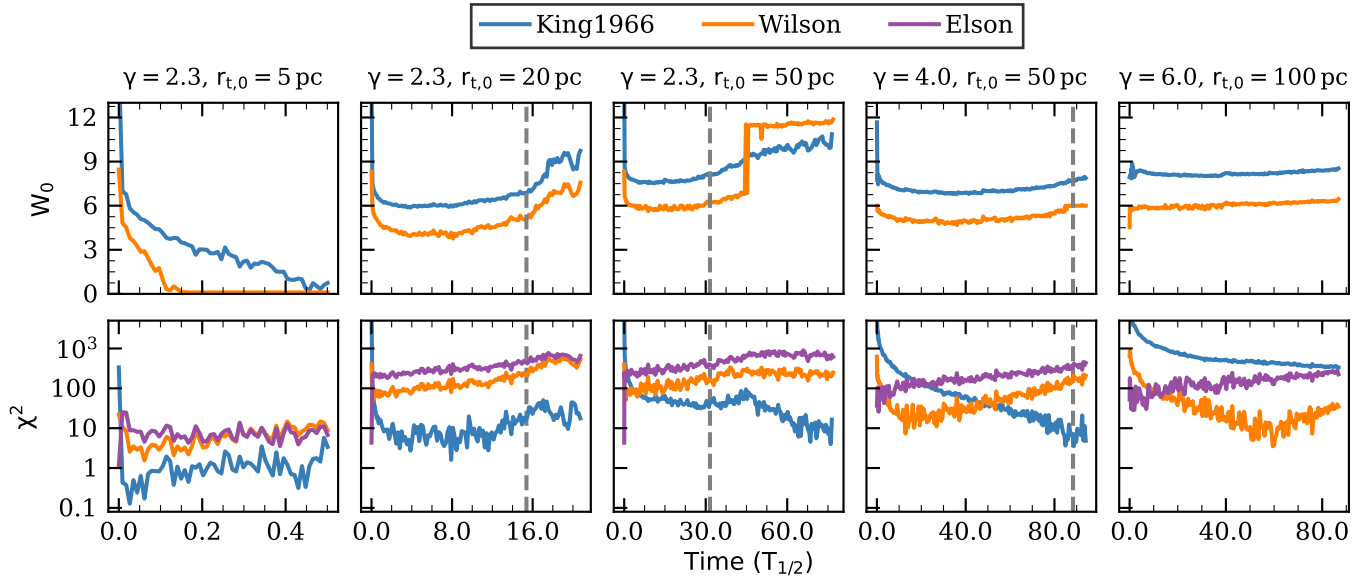


**Figure 2.** The best-fit values of  $W_0$  for King and Wilson profiles and the goodness of fit ( $\chi^2$ ) of those profiles (as well as the EFF profile, not shown) for a few representative clusters in `grid1`. All cluster models shown here have an initial virial radius of 1 pc. Clusters with tidal radii smaller than 100 pc become King-like before the simulation terminates. Conversely, clusters with  $r_{t,0} = 100$  pc have not had sufficient time to transition to a King profile and are best-fit by Wilson profiles. A vertical grey dashed line indicates when the cluster undergoes core collapse (i.e.  $N_{\text{BH}} < 10$ ), if applicable, and a distinct rise in  $W_0$  follows this event. A pre-core collapse  $W_0$  (value in bracket) is recorded in Table 1 for clusters that undergo core collapse.

The high density central regions of self-gravitating systems, such as star clusters, undergo a rapid and significant contraction. This collapse of their core happens due to the combined effect of two-body relaxation (Heggie & Hut 2003) and mass segregation (Spitzer 1987). Without counteracting mechanisms, massive objects tend to migrate towards the center of the gravitational potential, deepening the potential well and eventually leading to the collapse of the cluster. Binary systems within the core can undergo strong encounters with passing stars, resulting in the transfer of energy. During this process, the interacting star is expelled from the core, absorbing energy from the binary. The binary tightens due to the reduction in its energy, and the energy imparted to the interacting star is ultimately deposited in the outer halo of the cluster. This process of “binary burning” counteracts the gravitational collapse (e.g., Gao et al. 1991; Wilkinson et al. 2003; Chatterjee et al. 2010). BH binaries are generally the most massive systems with high potential energy and serve as efficient heat sources in this process.

However, BHs can be quickly ejected from cluster cores at the time of formation (primarily due to natal kicks) or later in their evolution through strong dynamical encounters (Morscher et al. 2015). If a cluster loses most of its BHs from the core, it loses the ability to remain heated and may eventually collapse anyway. For our analysis, we define a cluster as “core collapsed” if it

retains fewer than 10 stellar-mass BHs, as suggested in Kremer et al. (2018).

The core collapse manifests itself as a noticeable shift in the central surface brightness profile from flat core to a steep cusp. Some of the clusters with  $r_v = 1$  pc undergo core collapse, while none of those with  $r_v = 4$  pc experience it. Within 13.8 Gyr, when a cluster undergoes core collapse, the best-fit King and Wilson parameter,  $W_0$ , increases sharply (see Figure 2).

#### 4. TRANSITION FROM YMC TO GC

A star cluster, which begins its life having an EFF profile, starts immediately losing mass through its tidal boundary (which is not considered in the EFF density profile). Tidal mass loss through the outskirts coupled with the internal dynamical evolution changes the mass distribution of the cluster. Therefore, for a given cluster, the values of the fit parameters for density models change as the cluster evolves in time.

Figure 2 shows the evolution of the best fit parameter,  $W_0$ , for both King and Wilson models, and  $\chi^2$  values of the best-fit models for King, Wilson, and EFF models at each snapshot for a few representative clusters in `grid1` with  $r_v = 1$  pc. Typically, a cluster first transitions from an EFF profile to a Wilson profile, and eventually to a King profile. However, highly tidally truncated clusters (e.g.,  $r_{t,0} = 5$  pc) immediately transition to a King profile without going through a Wilson phase. On the other hand, tidally underfilling clusters

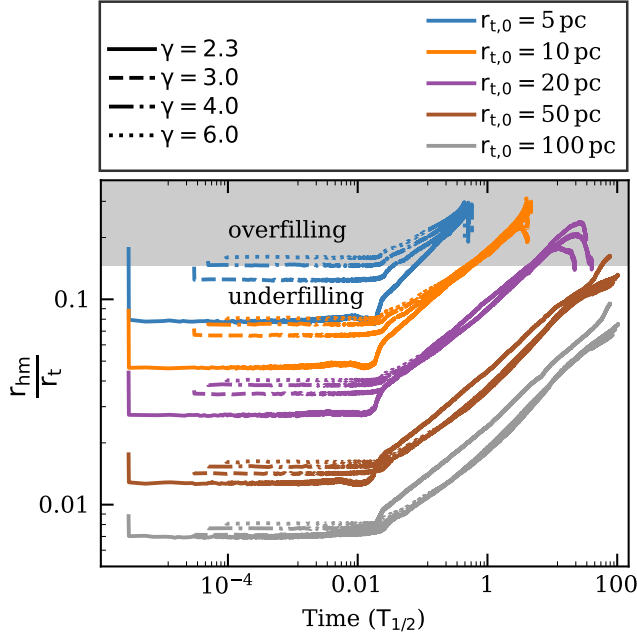


**Figure 3.** The evolution of the ratio of half-mass radius ( $r_{\text{hm}}$ ) and the instantaneous tidal radius ( $r_t$ ) of clusters with time. Here,  $T_{1/2}$  is the half-mass relaxation time of the cluster. All cluster models shown here have an initial virial radius of 1 pc. Tidally overfilling clusters ( $r_{\text{hm}}/r_t > 0.145$ ) are denoted by the shaded region. Notably, clusters with initial tidal radii ( $r_{t,0}$ ) smaller than 100 pc become King-like before the simulation terminates. Conversely, clusters with  $r_{t,0} = 100$  pc have not had sufficient time to transition to a King profile and are best-fit by Wilson models.

(e.g.,  $\gamma = 6.0$ ,  $r_{t,0} = 100$ ) never transition to a King profile. Table 1 records the disruption times, transition times for EFF  $\rightarrow$  Wilson and EFF  $\rightarrow$  King, and the King profile parameter  $W_0$  of the cluster if it has a King profile at the end of the simulation or its lifetime.

None of our clusters with  $r_v = 1$  pc and tidal radii  $\leq 20$  pc survive to the present day (13.8 Gyr), and spend most of their life best fit to a King profile. All clusters with tidal radii 50 pc survive and exhibit King profiles at the present day. The survival of these  $r_{t,0} \geq 50$  pc clusters to the present day ( $\sim 90 - 100 T_{1/2}$ ) approaches the evaporation times of isolated single-mass clusters (c.f. equation 7.141 and its discussion in Binney & Tremaine 2008), where  $T_{1/2}$  is the half-mass relaxation time of the cluster. With the exception of the  $\gamma = 2.3$  cluster, they spend approximately half of their existence better fit to a Wilson profile than a King profile. The majority of clusters with  $r_{t,0} = 100$  pc do not adopt King-like profiles by the present day, except for the  $\gamma = 2.3$  cluster. Initially, the density of an EFF profile cluster has a constant slope ( $\gamma$ ) at large radii. The dynamic evolution of the cluster begins to flatten the surface brightness pro-

file in the inner parts of the cluster, while tidal stripping in the outskirts brings about a sharp drop in the slope of the outer density profile over, with the density profile near the tidal boundary dropping to zero because the King (1966) profile is derived with an explicit energy cutoff (corresponding to the tidal boundary of the cluster).

The transition of a cluster from an EFF profile to a Wilson or King profile depends on whether the cluster is tidally underfilling or overfilling. A classic definition of tidal overfilling for a single mass model is when  $r_{\text{hm}}/r_t > 0.145$  (following Hénon 1961) where  $r_{\text{hm}}$  and  $r_t$  are the half-mass radius (the radius containing 50% of the mass of the cluster) and the instantaneous tidal radius of the cluster, respectively. A cluster with a higher  $r_{\text{hm}}/r_t$  ratio is considered tidally overfilling and should lose mass through the tidal boundary. Conversely, a cluster with a lower value of  $r_{\text{hm}}/r_t$  would be underfilling, and potentially not have evolved to a King model by the present day. As an example, Ye et al. (2022) was best able to reproduce the GC 47 Tuc by starting with an EFF profile with an initial profile slope of  $\gamma = 2.1$ . Their EFF model best fit the observational data of 47 Tuc at an age of 10.55 Gyr exhibiting a ratio of  $r_{\text{hm}}/r_t = 0.0436$  at that time. According to the above classic definition, this small value reaffirms that 47 Tuc is tidally underfilling and has not transitioned from an EFF to a King profile. Figure 3 shows the evolution of  $r_{\text{hm}}/r_t$  for the grid1 clusters. As a cluster evolves, dynamical heating causes the cluster to expand, increasing the  $r_{\text{hm}}/r_t$  ratio. All clusters with  $r_{t,0} < 50$  pc become tidally overfilling at some point before the end of the simulation and therefore should transition to a King profile. Indeed, we find that the  $\chi^2$  value for the fitted King model is smallest for any of the three models around the same time when the cluster enters the overfilling region in the  $r_{\text{hm}}/r_t - T_{1/2}$  plot. In Figure 3, most of the  $r_t = 50$  clusters never reach the overfilling region. However, based on  $\chi^2$  values, all  $r_t = 50$  clusters transition to the King profile before the end of the simulation. This discrepancy is likely due to the use of the classic definition of overfilling for our clusters. Our clusters have a realistic initial mass function (IMF) and undergo stellar evolution resulting in varying masses of cluster constituents. Consequently, the classic definition for overfilling, which assumes single-mass constituents and self-similar cluster models, is not strictly valid for these clusters.

For  $r_v = 1$  pc clusters, the transition time among clusters with the same tidal radius increases with a higher slope of the EFF profile. This happens because of two primary reasons – 1) smaller- $\gamma$  clusters are more extended, i.e. they have larger  $r_{\text{hm}}$  and evaporate com-



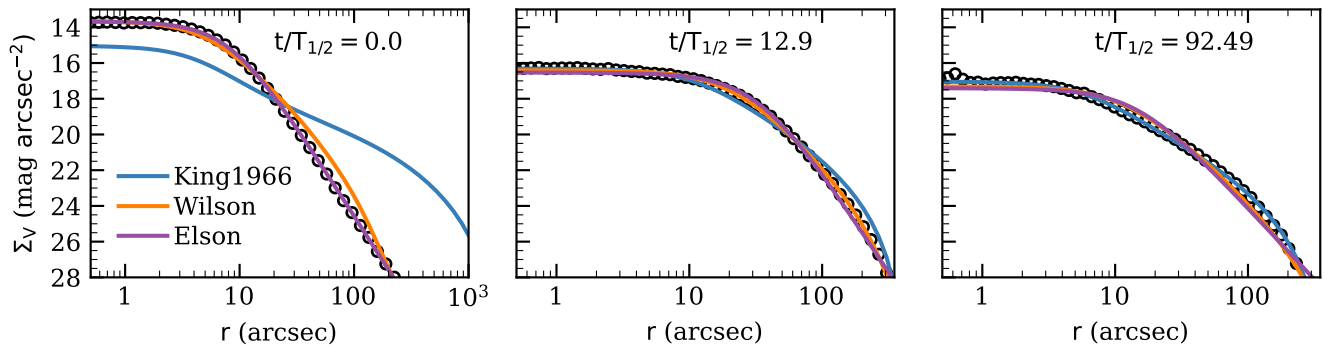


**Figure 4.** The transition of an EFF profile with time into a King profile for a cluster with  $\gamma = 4.0$ ,  $r_{t,0} = 50$  pc, and an initial virial radius of 1 pc. The radial location on the x-axis is given in arcseconds, assuming that the clusters are viewed at a nominal distance of 15 kpc. The *Left panel* shows the surface brightness profiles (open circles) and the corresponding fits for King, Wilson, and EFF models (color lines) at the beginning of the simulation. The *middle panel* and the *right panel* show the same information when the model has evolved to  $\sim 12.9 T_{1/2}$  and  $\sim 92.5 T_{1/2}$ , respectively. It is visually evident that the EFF, Wilson, and King models fit the surface brightness profile the best in the left, middle, and right panels, respectively.

paratively faster in the outer regions. 2) shallow EFF profiles have a higher central density, resulting in shorter relaxation times in the core region (c.f. equation 2.62 of Spitzer 1987). Therefore, clusters with small  $\gamma$  undergo a faster transformation in their inner structure as they are dynamically more active. Similarly, for a given slope of the EFF profile, clusters with larger tidal radii experience longer transition times because they evaporate slowly from the outskirts. Figure 4 shows the evolution of a typical cluster ( $\gamma = 4$ ,  $r_{t,0} = 50$  pc,  $r_v = 1$  pc) surface brightness profile at its three distinct evolutionary phases. This cluster transitions to a Wilson profile at  $\sim 6.45 T_{1/2}$  and eventually to a King profile at  $\sim 53.77 T_{1/2}$ . The general trends vis-à-vis the tidal radius and the slope of the EFF profile are similar for clusters with virial radii of 1 pc and 4 pc. For the same  $r_{t,0}$  and  $\gamma$ , a cluster with a smaller virial radius has a shorter relaxation time and therefore restructures its central regions faster. Therefore, the  $r_v = 4$  pc clusters have higher transition times for EFF  $\rightarrow$  Wilson and EFF  $\rightarrow$  King.

However, while the general trend in Figure 4 is that clusters take many half-mass relaxation times to transition to their most “King-like” or “Wilson-like”, it only takes a fraction of a  $T_{1/2}$  for a cluster to become more closely modeled by either profile than by its birth EFF profile. This is clearly seen in the bottom row of Figure 2. In Figure 5, we show the best-fit King and Wilson  $W_0$  parameters of the clusters as a function of the initial EFF  $\gamma$  parameter. Within  $0.2 T_{1/2}$ , the tidal truncation of the outer parts of the cluster largely dominated the best-fit  $W_0$  parameter for both profiles, erasing the initial correlation between  $\gamma$  and  $W_0$ . This suggests that, after only a fraction of the initial half-mass relaxation time, the  $W_0$  parameter is no longer a strong indicator

of the initial profile of the cluster (for systems with the same virial radii).

## 5. RUNAWAY COLLISIONS AND IMBH FORMATION

Since collisional runaways primarily occur in the earliest points of cluster evolution, clusters in grid2 are evolved for a maximum of 50 Myr. Once a BH forms from the collapse of its stellar counterpart, it has the potential for further growth through collisions with other stars or black holes. However, we are focused on the formation of massive black holes through the collapse of a single massive star formed via stellar runaway collisions. The growth of black holes from mergers of smaller black holes, extensively discussed in other works (e.g., Freitag et al. 2006; Umbreit et al. 2012; Rodriguez et al. 2018, 2019; Fragione & Silk 2020; Fragione et al. 2020, 2022), is not considered here. At a fixed virial radius, EFF clusters with smaller  $\gamma$  have denser and smaller cores (as seen in the right panel of Figure 1). Therefore, we expect such clusters to form the most massive IMBHs. Moreover, mass segregation during cluster evolution enhances the core density, further facilitating stellar encounters.

The Hénon monte Carlo method becomes unreliable when the mass of a single object within the cluster becomes a significant fraction of the total mass of the cluster. Given our clusters’ initial masses of  $3 \times 10^5$  and  $6 \times 10^5 M_\odot$ , with mass loss during evolution, we decided on a maximum cut-off mass of  $4000 M_\odot$  for a single object in the cluster. Therefore, we interrupt the simulations of clusters that form stars more massive than  $4000 M_\odot$ . Furthermore, some simulations terminate prematurely when a massive object ( $\sim 1000 M_\odot$ ) sinks very close to the center of the cluster potential ( $< 0.005$  pc). In such cases, the potential energy of the cluster changes

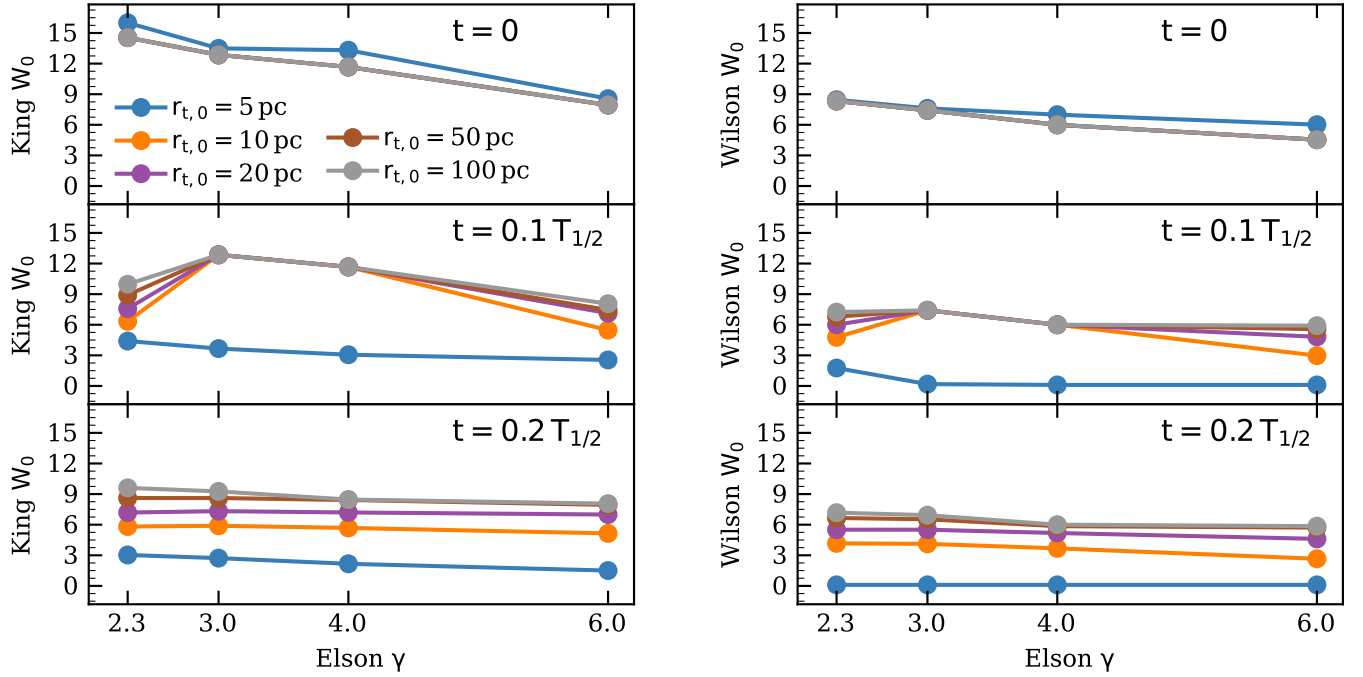


**Figure 5.** The best-fit  $W_0$  parameters for both King (left) and Wilson (right) profiles as a function of initial EFF  $\gamma$  parameter. We show the best-fit  $W_0$  parameters at 0, 0.1, and  $0.2 T_{1/2}$  from the cluster initialization. After  $0.2 T_{1/2}$  the  $W_0$  parameter of the cluster is largely dominated by the tidal radius, erasing the initial information about the power-law slope of the initial cluster.

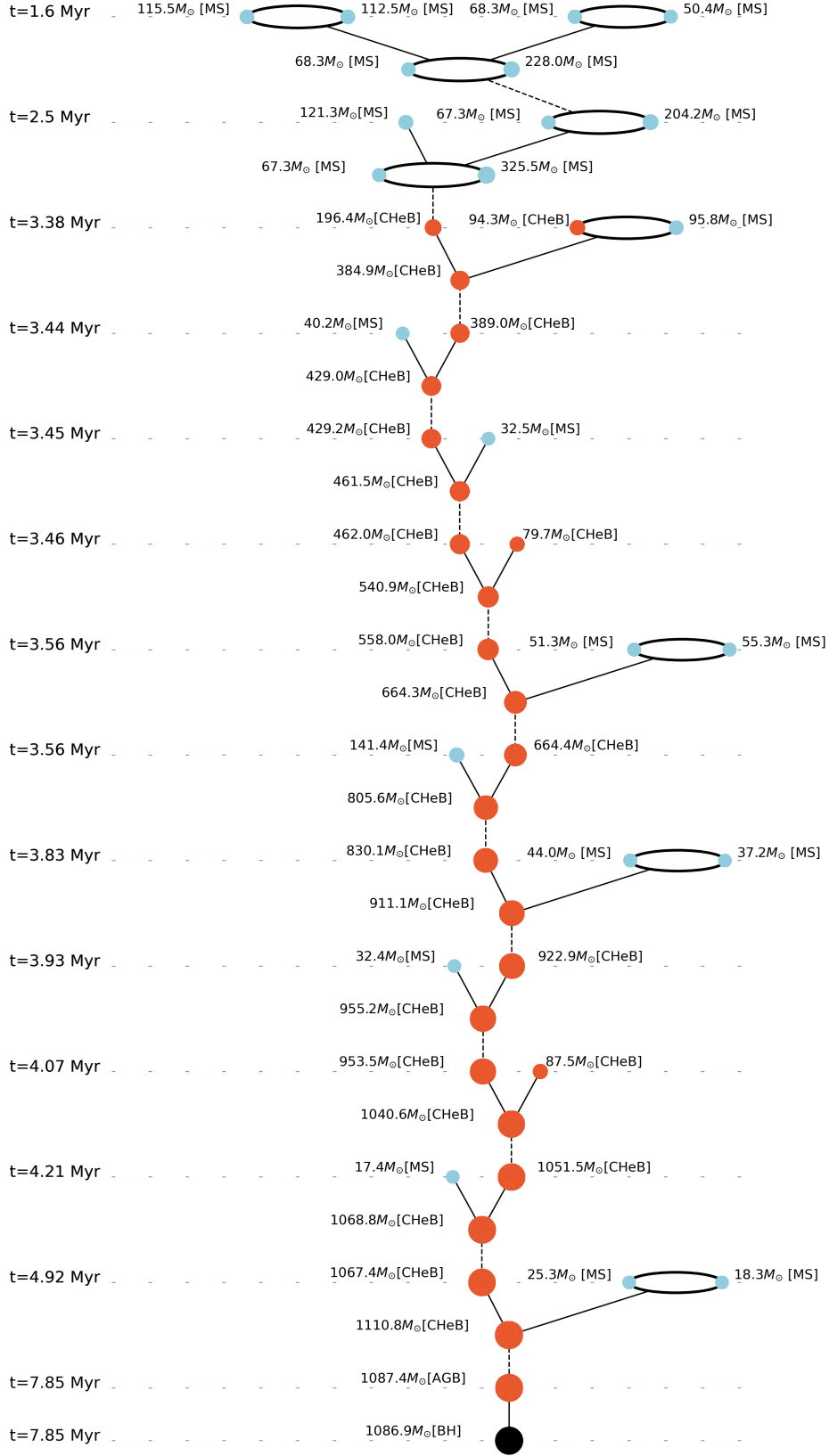
abruptly within a single time step due to the spherical symmetry of the code, causing the code to crash due to a significant jump in the energy. We indicate these in Tables 2 and 3 of the Appendix. In simulations where the most massive star has not collapsed into a BH before premature termination (marked by \* and †† in Tables 2 and 3), we subject it to standalone evolution (disregarding dynamical interactions) in COSMIC for a duration of up to 50 Myr by taking its instantaneous properties at the time of simulation termination as the initial conditions. We reiterate that because our simulations are terminated whenever a star becomes more massive than  $4000 M_\odot$ , that our BHs with masses in that range should be considered as lower limits.

Figure 6 shows the merger tree for a typical IMBH formed in our simulations. The interaction of two binaries with MS stars and component masses of  $(M_1, M_2) = (115.5 M_\odot, 112.5 M_\odot)$  and  $(68.3 M_\odot, 50.4 M_\odot)$  marks the beginning of the runaway process. This interaction results in the coalescence of the first binary into a  $228 M_\odot$  MS star, which captures the  $68.3 M_\odot$  star from the second binary. The product binary then collides with a MS single star of mass  $121.3 M_\odot$  and the primary star merges with the incoming single star, forming a  $325.5 M_\odot$  primary star. A series of further single-single and binary-single collisions lead to the formation of a  $1087.4 M_\odot$  asymptotic giant branch (AGB) star, which then collapses into an IMBH of mass  $1086.9 M_\odot$ . The

formation of this IMBH involves 1250 single-single, 11 binary-single, and 1 binary-binary encounters. Single-single, binary-single, and binary-binary encounters contribute 54.4%, 37.2%, and 8.4% of the total mass growth through collisions leading up to the formation of the IMBH, respectively.

We tabulate key simulation parameters and BH formation results in Table 2 (Table 3) in the Appendix for our collisional runaway grid for clusters with  $10^6$  ( $5 \times 10^5$ ) stars. We used two different prescriptions for collisions involving giant stars, CE0 and CE2, discussed in Section 2. In the CE2 prescription, more envelope mass is lost during a collision involving giant stars compared to the CE0 prescription. Therefore we see that stars in the CE0 prescription simulations are generally more massive than the CE2 prescription simulations and form the most massive IMBHs. In Figures 7 and 8, we display the masses of the most massive stars and BHs formed in our simulations with  $10^6$  particles for the CE0 and CE2 prescription, respectively.

For a given cluster size and profile slope  $\gamma$ , clusters with higher initial binary fraction ( $f_{b,h}$ ) form more massive IMBHs due to increased binary-mediated stellar collisions, aligning with the findings of González et al. (2021). For a given cluster size and initial  $f_{b,h}$ , clusters with denser cores (smaller  $\gamma$ ) form more massive IMBHs. Conversely, clusters with larger initial virial radii have fewer interactions for objects in the core and form less



**Figure 6.** The collision tree for a  $1086.9 M_{\odot}$  IMBH in a star cluster simulation with  $r_v = 2$  pc, Elson  $\gamma = 2.3$ , and  $f_{b,h} = 1.0$ . The size of the markers is proportional to the mass of the star, and binary stars are depicted in elliptical orbits. The MS stars are represented by blue, advanced evolutionary phases such as Core Helium Burning (CHeB) and AGB stars by red markers, and BHs by black markers. The physical time (in Myr) is shown on the left as the runaway collision progresses. The formation of this IMBH involves 1250 single-single, 11 binary-single, and 1 binary-binary encounters. Mergers with stars of mass  $< 10 M_{\odot}$  are not shown in this plot and are cumulatively represented by dashed lines.

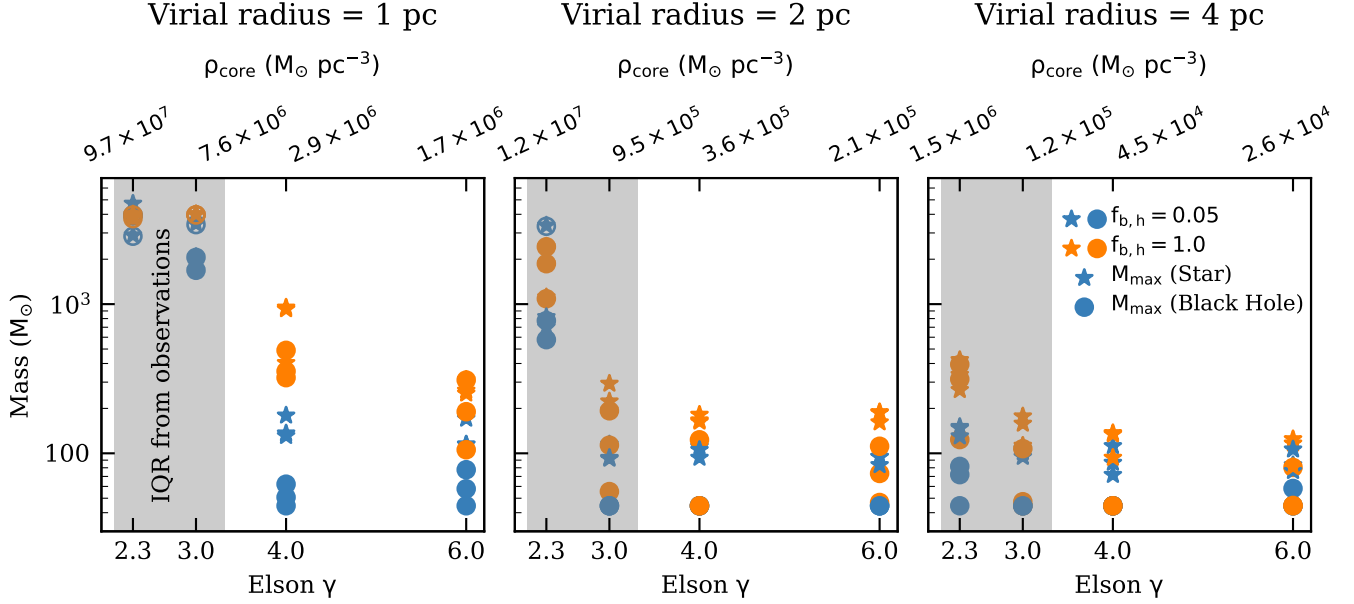


**Figure 7.** The maximum stellar and BH masses for  $N = 10^6$  star cluster simulations with the CE0 prescription. Each panel corresponds to simulations with different initial virial radii. Within each panel there are six simulations for each  $\gamma$ , representing three independent realizations for each high-mass binary fraction  $f_{b,h}$ . The upper horizontal axis displays the core density of the star cluster for a given  $\gamma$ . The shaded region indicates the Inter Quartile Range (IQR) (range between 25<sup>th</sup> and 75<sup>th</sup> percentile) of  $\gamma$  values of the suggested universal CDF of EFF slopes for young star clusters from Grudić et al. (2021). Open circles represent cluster simulations where — 1) either a  $4000 M_{\odot}$  star forms, or 2) the simulation terminates prematurely due to terminal energy error and the massive star has not collapsed by that time. For the *Left panel*, all clusters with  $\gamma = 2.3$  either form a  $4000 M_{\odot}$  star or encounter premature termination due to terminal energy error. Note that the most massive star in a simulation does not necessarily collapse to become the most massive BH in that simulation.

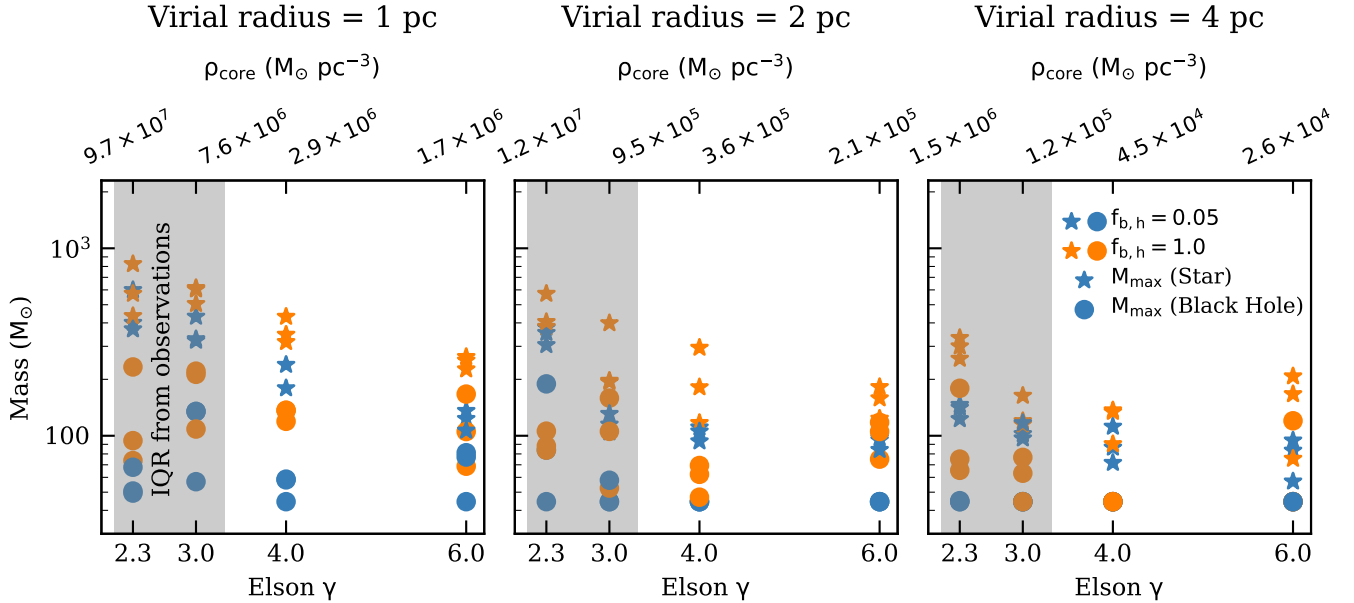


**Figure 8.** Same as Figure 7, but for the CE2 prescription. As expected, the masses are consistently smaller for the CE2 prescription compared to the CE0 prescription. However, the general trend with  $\gamma$  and the virial radius remains similar for both prescriptions.

massive (or no) IMBHs. The most massive stars formed in the CE0 prescription simulations with  $N = 10^6$  are  $4000 M_{\odot}$  (our simulation termination criterion) and the most massive BHs have similar masses. For the CE2 prescription simulations, the most massive star has a mass of  $824 M_{\odot}$  which collapses into a  $232.8 M_{\odot}$  IMBH.

All simulations in `grid2` form several BHs in the upper mass gap within any given cluster. Multiple IMBHs are observed in 13 out of 72 clusters for  $N = 10^6$  ( $M_{\text{cluster}} \simeq 6 \times 10^5 M_{\odot}$ ) clusters using the CE0 prescription, with the highest number (7) occurring in the cluster with  $\gamma = 4.0$ ,  $r_v = 1 \text{ pc}$ ,  $f_{b,h} = 1.0$ . Whereas, for  $N = 10^6$  and the CE2 prescription simulations, only 1 out of 72 clusters forms more than one IMBH. For  $N = 5 \times 10^5$ , the number of clusters forming multiple IMBHs within a single cluster is 5 and 1 for the CE0 and CE2 prescriptions, respectively. Notably, the highest number of IMBHs forms in a  $\gamma = 4.0$  cluster, while the most massive IMBHs form in  $\gamma = 2.3$  clusters.

### 5.1. Consequences for Long-term Cluster Evolution

From Tables 2 and 3, it becomes apparent that clusters with smaller values of  $\gamma$ , while keeping other initial conditions fixed, produce considerably fewer stellar-mass BHs. For instance, our  $N = 10^6$ ,  $f_{b,h} = 0.05$ ,  $r_v = 1 \text{ pc}$  clusters with  $\gamma = 2.3$  form  $\sim 20\%$  fewer stellar-mass BHs compared to  $\gamma = 6.0$  clusters. Dynamical interactions among these BHs often result in their expulsion from the cluster core (e.g., Breen & Hoggie 2013; Morscher et al. 2015). The right panel of Figure 9, shows the cumulative number of collisions ( $N_{\text{coll}}$ ) in  $N = 10^6$  star simulations with the CE2 prescription at 50 Myr. For  $f_{b,h} = 0.05$ , the ratio of average  $N_{\text{coll}}$  between  $\gamma = 2.3$  and  $\gamma = 6.0$  clusters is 12.06, 16.37, and 16.26 for  $r_v = 1, 2$ , and  $4 \text{ pc}$  clusters, respectively. For  $f_{b,h} = 1.0$ , this ratio is 9.4, 18.02, and 23.14, respectively. These collisions are largely between massive stars, the progenitors of stellar-mass BHs, meaning that smaller- $\gamma$  clusters produce fewer BHs. This is evident from the left panel of Figure 9 which shows the total number of BHs retained at 50 Myr in these clusters. For  $f_{b,h} = 0.05$ , the ratio of average  $N_{\text{BH}}$  between  $\gamma = 2.3$  and  $\gamma = 6.0$  clusters is 0.66, 0.78, and 0.82 for  $r_v = 1, 2$ , and  $4 \text{ pc}$  clusters, respectively. For  $f_{b,h} = 1.0$ , this ratio is 0.62, 0.73, and 0.83, respectively. The total number of BHs remaining in  $f_{b,h} = 1.0$  simulations is consistently higher than in  $f_{b,h} = 0.05$  simulations. It is interesting to note that  $\gamma \leq 3.0$  star clusters form and retain fewer stellar-mass BHs compared to  $\gamma = 6.0$  clusters of the same size but the most massive IMBHs are formed in these centrally dense star clusters. Although not shown, similar trends are exhibited by CE0 simulations.

As has been shown previously (Breen & Hoggie 2013; Kremer et al. 2018; Kremer et al. 2020a), the eventual *observational* core collapse of clusters is largely driven by the expulsion of their stellar-mass BH populations. This can occur in clusters that either dynamically eject their BHs by the present day (if they have sufficiently short  $T_{1/2}$ , e.g. Kremer et al. 2019), or in clusters that are born with fewer BHs to begin with (e.g., Rodriguez et al. 2023). What this suggests is that the very process of creating an IMBH through runaway collisions can deplete the cluster of stellar-mass BHs, and significantly accelerate core collapse! Ironically, our results are in agreement with the conventional wisdom that core-collapsed clusters may host IMBHs due to their extreme central densities. However, instead of the central density being responsible for IMBH formation, we argue that it is IMBH formation that leads to core collapse, and the high central density! Of course, just because a cluster lost its BH-progenitor stars in a collisional runaway does not mean that the cluster still contains an IMBH today (see González et al. 2022, which argues that IMBHs born with masses in the range  $120 - 500 M_{\odot}$  are ejected from the clusters within the first  $\sim 500$  Myr of evolution).

Our findings also align with previous studies by Hong et al. (2020) and Purohit et al. (2024), which demonstrate that the rate of binary BH mergers in clusters decreases with higher central densities and stronger runaway processes. This is in contrast with the slow scenario of IMBH formation, where the initial core collapse of the cluster increases the central density (e.g., Greene et al. 2020; Antonini et al. 2019), facilitating a higher number of collisions and the eventual formation of an IMBH. In our fast scenario, the presence of an IMBH expedites the core collapse process within the cluster.

## 6. DISCUSSION AND CONCLUSIONS

In this work, we have studied the dynamical evolution of young star clusters which are born with an EFF density profiles, similar to observations of young star clusters in the local universe. We have used two simulation grids with diverse sets of cluster initial conditions - `grid1` consisting 40 star cluster models to study the evolution of young EFF profile to old King profiles, and `grid2` consisting 288 star cluster models to explore the formation of IMBHs. In particular, we focus solely on the evolution of the cluster and formation of massive BHs within the initial 50 Myr. Our main conclusions are:

- 1) We have demonstrated that initially tidally overfilling EFF clusters transform to Wilson or King profiles through natural dynamical evolution. If and when a cluster transitions from an EFF profile to a Wilson or King profile depends on factors such as tidal filling,

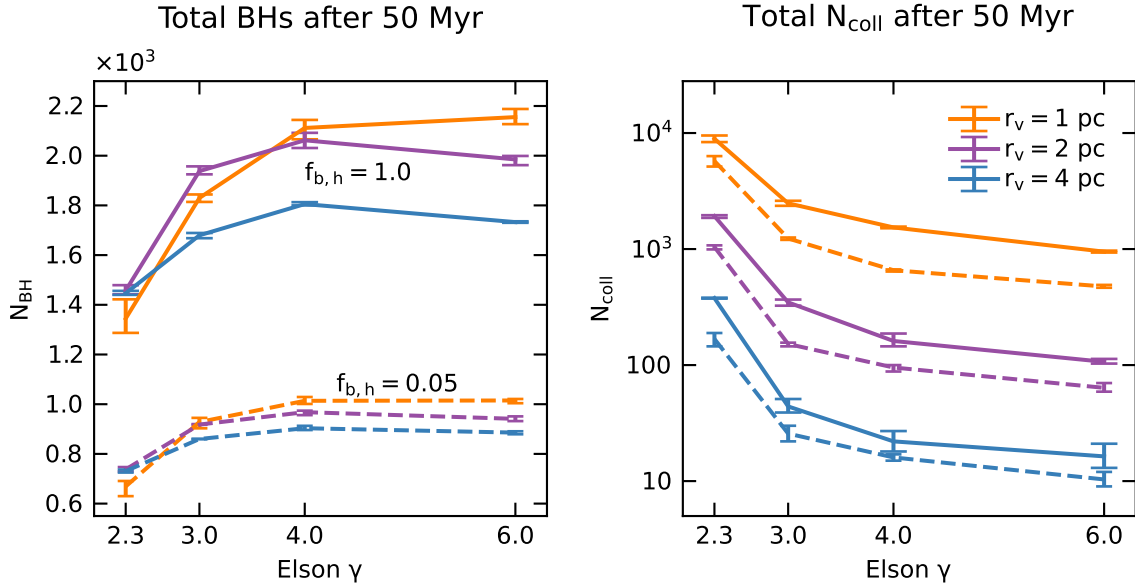


**Figure 9.** *Left panel:* shows the number of BHs in  $N = 10^6$  cluster simulations for the CE2 prescription. Solid (dashed) curves represent the average number of BHs for each  $\gamma$  with  $f_{\text{b,h}}$  of 1.0 (0.05). Each data point shows the range of  $N_{\text{BH}}$  formed in clusters of a given  $\gamma$  for three independent realizations. Clusters with higher core densities (smaller  $\gamma$ ), where massive BHs form and grow rapidly, tend to form a smaller number of BHs. *Right panel:* shows the total number of collisions upto 50 Myr for these simulations.

virial radius, and the initial slope of the EFF profile of the cluster. However, we show that while it may take many half-mass relaxation times for a cluster to become well-described by a King or Wilson profile, it only takes a fraction of that time for it to lose the memory of its initial EFF profile, suggesting that the King / Wilson parameter  $W_0$  of most clusters at the present day are not a good indicator of initial cluster profile or potential IMBH formation.

- 2) We find that massive EFF clusters with shallow density profiles can produce runaway stellar mergers with masses as high as  $4000 M_{\odot}$ . These massive stars collapse to form IMBHs with masses an order of magnitude higher than IMBHs produced in previous studies which assumed that young star clusters have a King profile (González et al. 2022, 2021; Kremer et al. 2020b). We find multiple clusters hosting several IMBHs, and the number of such clusters strongly correlates with the initial mass of the cluster & high-mass binary fraction, and the collision prescription used for interactions involving giant stars.
- 3) In centrally dense clusters characterized by smaller values of  $\gamma$ , the formation and growth of a collisional runaway star (and a subsequent IMBH) can reduce the number of stellar-mass BHs by nearly 40%. This trend suggests that the formation and retention of fewer stellar-mass BHs in clusters with

smaller  $\gamma$  values may accelerate the process of core collapse within these clusters. This in turn suggests that core-collapsed clusters may have been the site of IMBH formation at some point because the process of IMBH formation itself helped accelerate their core collapse.

Our study has relied on several assumptions for the outcomes of stellar collisions and massive star evolution, which we must address. First, we adopted two different collision prescriptions for stellar collisions involving giant stars and, unsurprisingly, find that more massive black holes are formed when using the “sticky sphere” collision prescription; i.e., CE0. However, the reality likely lies somewhere between the two collision prescriptions, CE0 and CE2. Our work emphasizes the importance of understanding the collision mechanism of massive stars. Accurate modeling of giant stellar collisions is highly uncertain, but recently it has been attempted by Costa et al. (2022) and Ballone et al. (2022) using hydrodynamical codes. However, these studies are limited in scope as they focus on specific encounter scenarios. Further work is required to accurately classify the properties of merger products in general collision scenarios, involving various stellar types, stellar masses, impact parameters, and collision velocities.

When a star comes in close proximity to a compact object, the outcome of the interaction depends on the impact parameter, as well as the masses, types, and ap-

proach velocities of the interacting objects. CMC does not yet have an extensive formalism to accurately model such collisions. By default, a star colliding with a BH in CMC results in the complete disruption of the star, termed a TDE (see Gezari 2021, for a review of TDEs). However, this is not a realistic prescription if, for instance, a  $5 M_{\odot}$  BH with a high relative velocity shoots through the loosely bound envelope of a giant star, as the giant star will probably lose only a small fraction of its mass. Therefore, we have used an ad hoc prescription (described in section 2) to avoid some of these situations. However, we emphasize that accurate modeling of TDEs is necessary, and efforts are currently underway.

Massive stars can undergo thousands of collisions, resulting in the formation of massive stars that eventually collapse to form an IMBH. When two stars collide, the chemical composition of the resulting merger product changes as a result of the mixing of material from the stars. Consequently, the merged product exhibits a chemical composition distinct from that of either progenitor. The extent of mixing determines the enhancement in the lifetime of a star (Hurley et al. 2002; Breivik et al. 2020). A prolonged lifetime for a massive star would allow for a greater number of collisions with other objects, thereby increasing the mass of the remnant formed during the star’s eventual collapse.

We form stars with masses up to  $4000 M_{\odot}$  in our simulations, employing the stellar evolution prescriptions of COSMIC (Breivik et al. 2020). These prescriptions are based on interpolation and extrapolation formulae from the SSE and BSE packages, derived by Hurley et al. (2000); Hurley et al. (2002), which, in turn, are based on the grid of stellar evolution tracks computed by Pols et al. (1998) for masses ranging from  $0.5$  to  $50 M_{\odot}$ . Notably, detailed stellar evolution models exist only for stars with a maximum mass of a few hundred solar masses (e.g., BoOST (Szécsi et al. 2022), BPASS (Eldridge et al. 2017), MIST (Choi et al. 2016)). The maximum stellar radius during a star’s evolution can vary by  $1000 R_{\odot}$  and the mass of the remnant formed at the end of a star’s life can differ by  $20 M_{\odot}$  among these stellar evolution models (Figures 2 and 3 of Agrawal et al. 2022). Accurate modelling of stellar evolutionary processes for massive stars has significant implications, influencing the physical size of stars (which strongly affects collision probabilities) and the mass of the resulting compact remnant.

Observations of star-forming regions suggest that both the distribution of molecular gas collapsing to form stars and the newly formed stars are asymmetric and clumpy in nature (Goodwin & Whitworth 2004, and references therein). Therefore, ideally, the young star

clusters should be modeled with fractal initial conditions (Küpper et al. 2011). Using direct N-body simulations of  $10^4$  star clusters with masses in the range of  $10^3 - 3 \times 10^4 M_{\odot}$  and fractal initial conditions, Di Carlo et al. (2021) concluded that runaway stellar collisions efficiently produce BHs with masses  $> 100 M_{\odot}$  and these BHs are efficient in acquiring a companion BH. They found that more massive and metal-poor clusters are more efficient at producing IMBHs. However, using fractal initial conditions in a Hénon-type Monte Carlo code, such as CMC, which assumes spherical symmetry, is not feasible. Therefore, we have to use a spherically symmetric density profile representative of young star clusters, which may limit the number of collisions that occur naturally in fractal initial conditions.

In this study, we exclusively focused on clusters with 10% solar metallicity. The metallicity of a star impacts wind mass loss rates, especially for massive stars. Stars with lower metallicity exhibit smaller wind mass loss rates and can retain a larger fraction of their mass. For young star clusters, Di Carlo et al. (2020) demonstrates that 6% of BHs in lower metallicity clusters ( $Z = 0.0002$ ) have  $M > 60 M_{\odot}$  compared to less than 1% in higher metallicity clusters ( $Z = 0.02$ ). Furthermore, Shrivastava & Kremer (2022) found that the number of BHs with  $M > 44.5 M_{\odot}$  formed in low-metallicity clusters ( $Z = 0.1 Z_{\odot}$ ) can be 10 times as many as in high-metallicity clusters ( $Z = Z_{\odot}$ ). In future work, we intend to explore the impact of metallicity on the formation and properties of IMBHs by incorporating data on stellar physical sizes from the latest stellar evolution models for massive stars.

#### ACKNOWLEDGEMENTS

We are grateful to Elena González and Kyle Kremer for useful discussions. This work was supported by NSF Grant AST-2310362 and NASA ATP Grant 80NSSC22K0722. CR also acknowledges support from a Charles E. Kaufman Foundation New Investigator Research Grant, an Alfred P. Sloan Research Fellowship, and a David and Lucile Packard Foundation Fellowship.

## APPENDIX

**Table 2.** Relevant simulation parameters and outputs for grid2 cluster simulations with  $N = 10^6$  objects.

$\gamma$	$r_v$ (pc)	$f_{b,h}$	$N_{BH}$	$N_{PI}$	$N_{IM}$	$M_{BH,max}$ ( $M_\odot$ )	$M_{*,max}$ ( $M_\odot$ )	$\gamma$	$r_v$ (pc)	$f_{b,h}$	$N_{BH}$	$N_{PI}$	$N_{IM}$	$M_{BH,max}$ ( $M_\odot$ )	$M_{*,max}$ ( $M_\odot$ )
CE2								CE0							
2.3	1	0.05	2013	33	0	50.7	400.5	2.3	1	0.05	322	41	1	3965.3*	4007.5*
2.3	1	0.05	2009	31	0	49.4	598.9	2.3	1	0.05	375	35	1	3903.7*	4719.1*
2.3	1	0.05	2060	28	0	67.9	370.0	2.3	1	0.05	817	31	2	2851.2 <sup>††</sup>	2895.2 <sup>††</sup>
2.3	1	1.0	2821	55	0	73.7	572.1	2.3	1	1.0	498	40	1	3961.9*	4000.6*
2.3	1	1.0	2931	46	1	232.8	824.1	2.3	1	1.0	356	59	1	3956.5*	4000.0*
2.3	1	1.0	2889	54	0	94.2	435.2	2.3	1	1.0	928	64	1	3740.4 <sup>††</sup>	3784.0 <sup>††</sup>
3.0	1	0.05	2485	46	1	134.8	321.6	3.0	1	0.05	1776	61	1	2056.4	2074.6
3.0	1	0.05	2470	42	1	134.7	432.0	3.0	1	0.05	2446	71	1	1685.8	1691.0
3.0	1	0.05	2461	43	0	56.9	327.7	3.0	1	0.05	461	59	2	3410.2 <sup>††</sup>	3453.7 <sup>††</sup>
3.0	1	1.0	3713	56	1	212.7	614.2	3.0	1	1.0	1405	92	4	3957.3*	4000.1*
3.0	1	1.0	3635	67	0	108.6	505.0	3.0	1	1.0	504	80	3	3969.0*	4002.7*
3.0	1	1.0	3692	56	2	221.1	604.0	3.0	1	1.0	421	89	4	3958.6*	4000.4*
4.0	1	0.05	2618	57	0	44.5	130.8	4.0	1	0.05	2627	80	0	50.7	130.8
4.0	1	0.05	2625	64	0	58.2	179.3	4.0	1	0.05	2630	80	0	44.5	179.3
4.0	1	0.05	2621	68	0	58.7	239.2	4.0	1	0.05	2630	84	0	62.1	136.1
4.0	1	1.0	4153	97	1	136.4	431.5	4.0	1	1.0	4093	132	6	354.8	403.5
4.0	1	1.0	4208	80	1	136.9	316.5	4.0	1	1.0	4128	123	5	321.4	949.1
4.0	1	1.0	4088	90	0	119.4	346.2	4.0	1	1.0	4071	106	7	490.0	925.9
6.0	1	0.05	2550	73	0	44.5	123.0	6.0	1	0.05	2545	82	0	44.5	170.8
6.0	1	0.05	2543	72	0	81.2	135.8	6.0	1	0.05	2554	81	0	77.6	114.3
6.0	1	0.05	2554	72	0	77.0	106.6	6.0	1	0.05	2555	80	0	57.8	114.8
6.0	1	1.0	4100	94	0	105.3	263.4	6.0	1	1.0	4158	113	2	190.1	263.4
6.0	1	1.0	4096	74	0	68.8	226.2	6.0	1	1.0	4111	103	2	309.8	311.8
6.0	1	1.0	4181	94	1	166.8	252.0	6.0	1	1.0	4107	105	0	105.7	252.0
2.3	2	0.05	2198	54	0	83.9	377.3	2.3	2	0.05	729	64	1	3324.8 <sup>††</sup>	3368.4 <sup>††</sup>
2.3	2	0.05	2194	55	1	189.1	304.8	2.3	2	0.05	2226	69	1	577.9	702.0
2.3	2	0.05	2181	48	0	44.5	354.0	2.3	2	0.05	2220	68	1	775.4	819.8
2.3	2	1.0	3099	85	0	88.3	381.3	2.3	2	1.0	2558	91	1	2423.2 <sup>†</sup>	2433.6 <sup>†</sup>
2.3	2	1.0	3127	79	0	105.8	572.3	2.3	2	1.0	3217	90	3	1086.9	1112.6
2.3	2	1.0	3097	79	0	83.8	404.7	2.3	2	1.0	3259	95	3	1866.2	1872.3
3.0	2	0.05	2489	82	0	44.5	104.4	3.0	2	0.05	2493	86	0	44.5	92.1
3.0	2	0.05	2489	83	0	44.5	114.8	3.0	2	0.05	2494	88	0	44.5	114.8
3.0	2	0.05	2494	84	0	57.9	130.9	3.0	2	0.05	2496	86	0	44.5	93.3
3.0	2	1.0	3871	101	1	158.8	398.7	3.0	2	1.0	3846	108	0	55.4	194.8
3.0	2	1.0	3748	91	0	52.6	196.7	3.0	2	1.0	3852	106	0	113.4	223.0

**Table 2** continued



Table 2 (continued)

$\gamma$	$r_v$ (pc)	$f_{b,h}$	$N_{BH}$	$N_{PI}$	$N_{IM}$	$M_{BH,max}$ ( $M_\odot$ )	$M_{*,max}$ ( $M_\odot$ )	$\gamma$	$r_v$ (pc)	$f_{b,h}$	$N_{BH}$	$N_{PI}$	$N_{IM}$	$M_{BH,max}$ ( $M_\odot$ )	$M_{*,max}$ ( $M_\odot$ )
CE2								CE0							
3.0	2	1.0	3781	100	0	105.5	193.8	3.0	2	1.0	3863	115	1	192.7	293.2
4.0	2	0.05	2627	90	0	44.5	110.9	4.0	2	0.05	2629	91	0	44.5	110.9
4.0	2	0.05	2639	84	0	44.5	93.4	4.0	2	0.05	2633	92	0	44.5	93.5
4.0	2	0.05	2631	90	0	44.5	105.5	4.0	2	0.05	2631	91	0	44.5	105.5
4.0	2	1.0	3755	113	0	69.4	117.1	4.0	2	1.0	3921	120	1	123.2	166.4
4.0	2	1.0	3761	102	0	62.3	295.0	4.0	2	1.0	3744	107	0	44.5	163.3
4.0	2	1.0	3788	120	0	47.0	181.6	4.0	2	1.0	3936	123	0	44.5	181.6
6.0	2	0.05	2539	78	0	44.5	94.7	6.0	2	0.05	2539	80	0	44.5	94.7
6.0	2	0.05	2545	82	0	44.5	97.5	6.0	2	0.05	2538	80	0	44.5	95.0
6.0	2	0.05	2545	81	0	44.5	84.1	6.0	2	0.05	2542	81	0	44.5	83.5
6.0	2	1.0	3507	89	0	117.9	182.0	6.0	2	1.0	3482	92	0	73.3	187.3
6.0	2	1.0	3496	88	0	75.1	158.5	6.0	2	1.0	3454	95	0	46.8	161.4
6.0	2	1.0	3525	93	0	105.3	123.4	6.0	2	1.0	3545	86	0	111.5	188.9
2.3	4	0.05	2138	71	0	44.5	146.2	2.3	4	0.05	2139	71	0	72.0	150.4
2.3	4	0.05	2151	70	0	45.1	141.1	2.3	4	0.05	2146	72	0	44.5	147.7
2.3	4	0.05	2141	68	0	44.5	122.8	2.3	4	0.05	2143	73	0	81.7	130.1
2.3	4	1.0	3008	93	0	75.1	332.7	2.3	4	1.0	3026	99	1	123.6	265.8
2.3	4	1.0	3085	94	1	179.2	257.7	2.3	4	1.0	3046	111	3	314.2	336.1
2.3	4	1.0	3017	95	0	65.4	300.0	2.3	4	1.0	3052	102	1	394.4	422.4
3.0	4	0.05	2451	84	0	44.5	96.9	3.0	4	0.05	2446	84	0	44.5	107.1
3.0	4	0.05	2448	85	0	44.5	102.1	3.0	4	0.05	2441	84	0	44.5	102.1
3.0	4	0.05	2444	85	0	44.5	116.9	3.0	4	0.05	2444	85	0	44.5	94.8
3.0	4	1.0	3065	94	0	76.7	119.8	3.0	4	1.0	3063	91	0	44.5	177.0
3.0	4	1.0	3052	83	0	63.1	115.0	3.0	4	1.0	3104	85	0	47.4	112.6
3.0	4	1.0	3047	90	0	44.5	163.5	3.0	4	1.0	3125	85	0	107.5	158.2
4.0	4	0.05	2608	90	0	44.5	71.7	4.0	4	0.05	2612	91	0	44.5	71.7
4.0	4	0.05	2608	90	0	44.5	111.9	4.0	4	0.05	2602	90	0	44.5	111.9
4.0	4	0.05	2615	91	0	44.5	86.6	4.0	4	0.05	2620	90	0	44.5	86.5
4.0	4	1.0	3307	89	0	44.5	136.7	4.0	4	1.0	3324	93	0	44.5	136.7
4.0	4	1.0	3333	95	0	44.5	134.2	4.0	4	1.0	3334	105	0	44.5	134.2
4.0	4	1.0	3293	96	0	44.5	90.2	4.0	4	1.0	3337	102	0	44.5	93.5
6.0	4	0.05	2520	81	0	44.5	83.4	6.0	4	0.05	2518	80	0	44.5	83.4
6.0	4	0.05	2512	80	0	44.5	57.1	6.0	4	0.05	2521	79	0	44.5	76.2
6.0	4	0.05	2521	80	0	44.5	94.4	6.0	4	0.05	2510	82	0	58.1	106.3
6.0	4	1.0	3115	72	0	44.5	75.4	6.0	4	1.0	3121	69	0	80.4	124.5
6.0	4	1.0	3136	73	0	44.5	207.6	6.0	4	1.0	3127	71	0	44.5	116.5
6.0	4	1.0	3127	83	1	120.2	166.8	6.0	4	1.0	3115	80	0	44.7	81.1

Table 2 continued

**Table 2** (*continued*)

$\gamma$	$r_v$	$f_{b,h}$	$N_{BH}$	$N_{PI}$	$N_{IM}$	$M_{BH,max}$	$M_{*,max}$	$\gamma$	$r_v$	$f_{b,h}$	$N_{BH}$	$N_{PI}$	$N_{IM}$	$M_{BH,max}$	$M_{*,max}$
	(pc)					( $M_\odot$ )	( $M_\odot$ )		(pc)					( $M_\odot$ )	( $M_\odot$ )
CE2								CE0							

NOTE—These simulations have a metallicity of  $Z = 0.1 Z_\odot$ . The left and right halves of the table are for simulations with the CE2 and CE0 collision prescriptions, respectively. The columns in the table for each simulation include the initial Elson profile slope ( $\gamma$ ), virial radius ( $r_v$ ), high-mass binary fraction ( $f_{b,h}$ ); total number of BHs formed through stellar collapse ( $N_{BH}$ ), total number of BHs formed in the mass range  $44.5 - 120 M_\odot$  ( $N_{PI}$ ), total number of IMBHs ( $N_{IM}$ ), the most massive BH ( $M_{BH,max}$ ), and the most massive star ( $M_{*,max}$ ). Rows marked with an asterisk (\*) next to  $M_{BH,max}$  and  $M_{*,max}$  denote that a star more massive than  $4000.0 M_\odot$  formed during the simulation, leading to its termination before 50 Myr. Simulations that terminate prematurely due to terminal energy error (see text) are denoted by † or †† symbols next to the values in  $M_{BH,max}$  and  $M_{*,max}$  columns. Simulations which stop prematurely but have the most massive star collapsing to form a black hole are marked with †. For simulations ending prematurely due to energy error but with the most massive star yet to collapse, we use the †† symbol. In cases marked with \* or ††, we take the instantaneous properties of the most massive star at the time of simulation termination as initial conditions and evolve it in a standalone fashion (no dynamics) in COSMIC up to 50 Myr. In these cases, massive stars at the time of premature simulation termination are in core helium burning phase and that is why upon further standalone evolution using COSMIC they quickly collapse converting most of their mass into an IMBHs.

**Table 3.** Relevant simulation parameters and outputs for grid2 cluster simulations with  $N = 5 \times 10^5$  objects.

$\gamma$	$r_v$	$f_{b,h}$	$N_{BH}$	$N_{PI}$	$N_{IM}$	$M_{BH,max}$	$M_{*,max}$	$\gamma$	$r_v$	$f_{b,h}$	$N_{BH}$	$N_{PI}$	$N_{IM}$	$M_{BH,max}$	$M_{*,max}$
	(pc)					( $M_\odot$ )	( $M_\odot$ )		(pc)					( $M_\odot$ )	( $M_\odot$ )
CE2								CE0							
2.3	1	0.05	1011	13	0	46.7	362.5	2.3	1	0.05	1031	14	1	1063.6†	1080.4†
2.3	1	0.05	999	9	0	44.5	324.7	2.3	1	0.05	1053	10	1	925.6	1024.5
2.3	1	0.05	1016	10	0	83.8	412.8	2.3	1	0.05	159	16	1	1854.3††	1898.7††
2.3	1	1.0	1442	23	0	84.9	468.3	2.3	1	1.0	624	14	2	2378.8††	2422.6††
2.3	1	1.0	1348	26	1	136.8	380.1	2.3	1	1.0	241	23	1	2345.5††	2389.3††
2.3	1	1.0	1430	13	1	148.2	450.6	2.3	1	1.0	108	19	1	2754.6††	2798.4††
3.0	1	0.05	1240	27	0	44.5	223.8	3.0	1	0.05	1205	39	1	1103.0	1123.2
3.0	1	0.05	1230	25	1	162.1	245.7	3.0	1	0.05	261	39	1	2244.9††	2288.1††
3.0	1	0.05	1235	24	1	225.0	392.3	3.0	1	0.05	1239	39	1	799.0	811.9
3.0	1	1.0	1829	44	1	154.3	405.9	3.0	1	1.0	1860	50	2	849.8	876.1
3.0	1	1.0	1797	36	3	149.5	327.0	3.0	1	1.0	1820	55	2	410.6	722.0
3.0	1	1.0	1778	35	1	124.6	369.5	3.0	1	1.0	1550	53	2	1507.1†	1510.0†
4.0	1	0.05	1287	28	0	97.8	141.0	4.0	1	0.05	1280	41	0	104.4	157.8
4.0	1	0.05	1282	34	0	101.9	137.5	4.0	1	0.05	1282	38	0	44.5	145.8
4.0	1	0.05	1277	37	0	51.1	177.9	4.0	1	0.05	1283	40	0	44.5	128.8
4.0	1	1.0	2070	48	1	184.0	231.5	4.0	1	1.0	2090	59	0	95.7	296.1
4.0	1	1.0	2047	48	0	68.0	241.6	4.0	1	1.0	2079	57	0	96.8	295.0
4.0	1	1.0	2098	38	0	104.1	317.1	4.0	1	1.0	2044	62	2	179.3	298.5
6.0	1	0.05	1329	35	0	44.5	140.3	6.0	1	0.05	1324	35	0	44.5	139.9
6.0	1	0.05	1321	29	0	44.5	104.2	6.0	1	0.05	1327	38	0	44.5	99.6
6.0	1	0.05	1323	31	0	44.5	136.9	6.0	1	0.05	1323	41	0	46.2	136.9

**Table 3** *continued*

Table 3 (continued)

$\gamma$	$r_v$ (pc)	$f_{b,h}$	$N_{BH}$	$N_{PI}$	$N_{IM}$	$M_{BH,max}$ ( $M_\odot$ )	$M_{*,max}$ ( $M_\odot$ )	$\gamma$	$r_v$ (pc)	$f_{b,h}$	$N_{BH}$	$N_{PI}$	$N_{IM}$	$M_{BH,max}$ ( $M_\odot$ )	$M_{*,max}$ ( $M_\odot$ )
CE2								CE0							
6.0	1	1.0	2089	42	0	44.5	223.3	6.0	1	1.0	2090	52	1	295.1	328.4
6.0	1	1.0	2090	36	0	104.2	190.1	6.0	1	1.0	2131	57	1	173.7	227.6
6.0	1	1.0	2070	39	0	76.8	233.8	6.0	1	1.0	2113	58	1	184.7	214.1
2.3	2	0.05	1099	13	0	44.5	452.6	2.3	2	0.05	1101	19	1	328.2	482.2
2.3	2	0.05	1122	14	1	167.7	477.0	2.3	2	0.05	1097	22	1	450.6	459.3
2.3	2	0.05	1095	14	1	135.5	270.3	2.3	2	0.05	1125	21	0	44.5	622.0
2.3	2	1.0	1502	28	0	93.1	360.6	2.3	2	1.0	1541	31	1	458.9	518.6
2.3	2	1.0	1491	31	0	58.7	264.4	2.3	2	1.0	1543	50	0	112.0	449.1
2.3	2	1.0	1502	33	0	116.4	268.9	2.3	2	1.0	1551	52	1	137.8	486.5
3.0	2	0.05	1268	43	0	44.5	94.2	3.0	2	0.05	1257	45	0	44.5	112.3
3.0	2	0.05	1262	43	0	44.5	92.3	3.0	2	0.05	1262	46	0	44.5	103.7
3.0	2	0.05	1271	42	0	44.5	101.0	3.0	2	0.05	1267	44	0	44.5	93.8
3.0	2	1.0	1727	42	0	44.5	155.4	3.0	2	1.0	1777	49	0	44.5	140.8
3.0	2	1.0	1810	51	0	72.9	178.1	3.0	2	1.0	1817	56	0	90.0	216.8
3.0	2	1.0	1814	56	0	85.7	215.8	3.0	2	1.0	1786	54	0	118.7	173.1
4.0	2	0.05	1276	38	0	44.5	82.7	4.0	2	0.05	1276	41	0	44.5	88.3
4.0	2	0.05	1276	41	0	44.5	90.5	4.0	2	0.05	1285	39	0	44.5	90.5
4.0	2	0.05	1273	39	0	44.5	93.0	4.0	2	0.05	1271	40	0	44.5	93.0
4.0	2	1.0	1796	43	0	44.5	92.8	4.0	2	1.0	1749	40	0	44.5	155.3
4.0	2	1.0	1762	43	0	44.5	116.5	4.0	2	1.0	1790	50	0	44.5	124.6
4.0	2	1.0	1738	49	0	44.5	160.0	4.0	2	1.0	1780	49	0	45.6	160.0
6.0	2	0.05	1324	37	0	44.5	77.1	6.0	2	0.05	1319	40	0	44.5	130.9
6.0	2	0.05	1319	37	0	44.5	84.4	6.0	2	0.05	1317	39	0	44.5	65.5
6.0	2	0.05	1313	38	0	44.5	122.9	6.0	2	0.05	1321	38	0	44.5	122.9
6.0	2	1.0	1744	39	0	44.5	90.2	6.0	2	1.0	1762	38	0	44.5	90.6
6.0	2	1.0	1748	40	0	49.4	112.0	6.0	2	1.0	1765	39	0	44.5	162.3
6.0	2	1.0	1754	39	0	44.5	130.1	6.0	2	1.0	1737	38	0	44.5	130.1
2.3	4	0.05	1089	24	0	44.5	136.6	2.3	4	0.05	1090	26	0	44.5	162.7
2.3	4	0.05	1099	26	0	44.5	99.0	2.3	4	0.05	1094	29	0	44.5	95.3
2.3	4	0.05	1091	26	0	44.5	89.9	2.3	4	0.05	1088	26	0	44.5	141.2
2.3	4	1.0	1395	36	0	45.9	283.5	2.3	4	1.0	1413	38	0	94.0	233.7
2.3	4	1.0	1431	36	1	128.2	204.3	2.3	4	1.0	1400	41	0	44.5	281.4
2.3	4	1.0	1432	39	0	65.9	266.8	2.3	4	1.0	1518	39	1	298.4	343.8
3.0	4	0.05	1229	45	0	44.5	78.0	3.0	4	0.05	1230	45	0	44.5	80.5
3.0	4	0.05	1232	44	0	44.5	58.7	3.0	4	0.05	1228	45	0	44.5	86.4
3.0	4	0.05	1232	45	0	44.5	91.6	3.0	4	0.05	1227	45	0	44.5	91.6
3.0	4	1.0	1460	42	0	44.5	99.5	3.0	4	1.0	1468	43	0	44.5	70.1
3.0	4	1.0	1459	51	0	44.5	84.1	3.0	4	1.0	1486	50	0	44.5	82.9

Table 3 continued

Table 3 (continued)

$\gamma$	$r_v$ (pc)	$f_{b,h}$	$N_{BH}$	$N_{PI}$	$N_{IM}$	$M_{BH,max}$ ( $M_\odot$ )	$M_{*,max}$ ( $M_\odot$ )	$\gamma$	$r_v$ (pc)	$f_{b,h}$	$N_{BH}$	$N_{PI}$	$N_{IM}$	$M_{BH,max}$ ( $M_\odot$ )	$M_{*,max}$ ( $M_\odot$ )
CE2								CE0							
3.0	4	1.0	1495	50	0	44.5	113.8	3.0	4	1.0	1453	51	0	44.5	96.0
4.0	4	0.05	1270	39	0	44.5	89.7	4.0	4	0.05	1271	38	0	44.5	69.4
4.0	4	0.05	1273	36	0	44.5	42.7	4.0	4	0.05	1272	38	0	44.5	57.0
4.0	4	0.05	1269	38	0	44.5	44.9	4.0	4	0.05	1274	38	0	44.5	70.6
4.0	4	1.0	1552	39	0	44.5	94.6	4.0	4	1.0	1572	39	0	44.5	94.6
4.0	4	1.0	1554	37	0	44.5	64.4	4.0	4	1.0	1574	37	0	44.5	64.4
4.0	4	1.0	1562	34	0	44.5	105.2	4.0	4	1.0	1553	37	0	44.5	59.5
6.0	4	0.05	1311	38	0	44.5	79.8	6.0	4	0.05	1311	39	0	44.5	24.3
6.0	4	0.05	1307	38	0	44.5	55.4	6.0	4	0.05	1311	38	0	44.5	56.2
6.0	4	0.05	1313	39	0	44.5	29.6	6.0	4	0.05	1313	39	0	44.5	29.6
6.0	4	1.0	1570	37	0	44.5	57.3	6.0	4	1.0	1574	36	0	44.5	57.2
6.0	4	1.0	1552	39	0	44.5	50.8	6.0	4	1.0	1560	39	0	44.5	67.3
6.0	4	1.0	1555	39	0	44.5	80.8	6.0	4	1.0	1536	39	0	44.5	80.8

NOTE—Please refer to the note of Table 2 for the interpretation of symbols such as † and †† in columns  $M_{BH,max}$  and  $M_{*,max}$ .

## REFERENCES

- Aasi, J., Abbott, B. P., Abbott, R., Abbott, T., & Abernathy, M. R. 2015, *Classical and Quantum Gravity*, 32, 074001, doi: [10.1088/0264-9381/32/7/074001](https://doi.org/10.1088/0264-9381/32/7/074001)
- Acernese, F., Agathos, M., Agatsuma, K., Aisa, D., & Allemandou, N. 2014, *Classical and Quantum Gravity*, 32, 024001, doi: [10.1088/0264-9381/32/2/024001](https://doi.org/10.1088/0264-9381/32/2/024001)
- Agrawal, P., Szécsi, D., Stevenson, S., Eldridge, J. J., & Hurley, J. 2022, *MNRAS*, 512, 5717, doi: [10.1093/mnras/stac930](https://doi.org/10.1093/mnras/stac930)
- Antonini, F., Gieles, M., & Gualandris, A. 2019, *MNRAS*, 486, 5008, doi: [10.1093/mnras/stz1149](https://doi.org/10.1093/mnras/stz1149)
- Ballone, A., Costa, G., Mapelli, M., & MacLeod, M. 2022, arXiv e-prints, arXiv:2204.03493. <https://arxiv.org/abs/2204.03493>
- Banerjee, S. 2021, *MNRAS*, 500, 3002, doi: [10.1093/mnras/staa2392](https://doi.org/10.1093/mnras/staa2392)
- Banerjee, S., Belczynski, K., Fryer, C. L., et al. 2020, *A&A*, 639, A41, doi: [10.1051/0004-6361/201935332](https://doi.org/10.1051/0004-6361/201935332)
- Barkat, Z., Rakavy, G., & Sack, N. 1967, *Phys. Rev. Lett.*, 18, 379, doi: [10.1103/PhysRevLett.18.379](https://doi.org/10.1103/PhysRevLett.18.379)
- Bastian, N., Schweizer, F., Goudfrooij, P., Larsen, S. S., & Kissler-Patig, M. 2013, *MNRAS*, 431, 1252, doi: [10.1093/mnras/stt253](https://doi.org/10.1093/mnras/stt253)
- Belczynski, K., Heger, A., Gladysz, W., et al. 2016, *A&A*, 594, A97, doi: [10.1051/0004-6361/201628980](https://doi.org/10.1051/0004-6361/201628980)
- Binney, J., & Tremaine, S. 2008, *Galactic Dynamics: Second Edition*
- Breen, P. G., & Heggie, D. C. 2013, *MNRAS*, 432, 2779, doi: [10.1093/mnras/stt628](https://doi.org/10.1093/mnras/stt628)
- Breivik, K., Coughlin, S., Zevin, M., et al. 2020, *ApJ*, 898, 71, doi: [10.3847/1538-4357/ab9d85](https://doi.org/10.3847/1538-4357/ab9d85)
- Bromm, V., & Larson, R. B. 2004, *ARA&A*, 42, 79, doi: [10.1146/annurev.astro.42.053102.134034](https://doi.org/10.1146/annurev.astro.42.053102.134034)
- Bromm, V., & Loeb, A. 2003, *ApJ*, 596, 34, doi: [10.1086/377529](https://doi.org/10.1086/377529)
- Carr, B., Kühnel, F., & Sandstad, M. 2016, *PhRvD*, 94, 083504, doi: [10.1103/PhysRevD.94.083504](https://doi.org/10.1103/PhysRevD.94.083504)
- Chatterjee, S., Fregeau, J. M., Umbreit, S., & Rasio, F. A. 2010, *ApJ*, 719, 915. [http://adsabs.harvard.edu/cgi-bin/nph-data\\_query?bibcode=2010ApJ...719..915C&link\\_type=EJOURNAL](http://adsabs.harvard.edu/cgi-bin/nph-data_query?bibcode=2010ApJ...719..915C&link_type=EJOURNAL)
- Choi, J., Dotter, A., Conroy, C., et al. 2016, *ApJ*, 823, 102, doi: [10.3847/0004-637X/823/2/102](https://doi.org/10.3847/0004-637X/823/2/102)
- Costa, G., Ballone, A., Mapelli, M., & Bressan, A. 2022, *MNRAS*, 516, 1072, doi: [10.1093/mnras/stac2222](https://doi.org/10.1093/mnras/stac2222)
- Di Carlo, U. N., Giacobbo, N., Mapelli, M., et al. 2019, *MNRAS*, 487, 2947, doi: [10.1093/mnras/stz1453](https://doi.org/10.1093/mnras/stz1453)
- Di Carlo, U. N., Mapelli, M., Giacobbo, N., et al. 2020, *MNRAS*, 498, 495, doi: [10.1093/mnras/staa2286](https://doi.org/10.1093/mnras/staa2286)

- Di Carlo, U. N., Mapelli, M., Pasquato, M., et al. 2021, *MNRAS*, 507, 5132, doi: [10.1093/mnras/stab2390](https://doi.org/10.1093/mnras/stab2390)
- Eldridge, J. J., Stanway, E. R., Xiao, L., et al. 2017, *PASA*, 34, e058, doi: [10.1017/pasa.2017.51](https://doi.org/10.1017/pasa.2017.51)
- Elson, R. A. W., Fall, S. M., & Freeman, K. C. 1987, *ApJ*, 323, 54, doi: [10.1086/165807](https://doi.org/10.1086/165807)
- Fragione, G., Kocsis, B., Rasio, F. A., & Silk, J. 2022, *ApJ*, 927, 231, doi: [10.3847/1538-4357/ac5026](https://doi.org/10.3847/1538-4357/ac5026)
- Fragione, G., Loeb, A., & Rasio, F. A. 2020, *ApJL*, 902, L26, doi: [10.3847/2041-8213/abbc0a](https://doi.org/10.3847/2041-8213/abbc0a)
- Fragione, G., & Silk, J. 2020, *MNRAS*, 498, 4591, doi: [10.1093/mnras/staa2629](https://doi.org/10.1093/mnras/staa2629)
- Freitag, M., Amaro-Seoane, P., & Kalogera, V. 2006, *ApJ*, 649, 91, doi: [10.1086/506193](https://doi.org/10.1086/506193)
- Fryer, C. L., Belczynski, K., Wiktorowicz, G., et al. 2012, *ApJ*, 749, 91, doi: [10.1088/0004-637X/749/1/91](https://doi.org/10.1088/0004-637X/749/1/91)
- Fryer, C. L., Woosley, S. E., & Heger, A. 2001, *ApJ*, 550, 372, doi: [10.1086/319719](https://doi.org/10.1086/319719)
- Gao, B., Goodman, J., Cohn, H., & Murphy, B. 1991, *ApJ*, 370, 567, doi: [10.1086/169843](https://doi.org/10.1086/169843)
- Gatto, M., Ripepi, V., Bellazzini, M., et al. 2021, *MNRAS*, 507, 3312, doi: [10.1093/mnras/stab2297](https://doi.org/10.1093/mnras/stab2297)
- Gezari, S. 2021, *ARA&A*, 59, 21, doi: [10.1146/annurev-astro-111720-030029](https://doi.org/10.1146/annurev-astro-111720-030029)
- González, E., Kremer, K., Chatterjee, S., et al. 2021, *ApJL*, 908, L29, doi: [10.3847/2041-8213/abdf5b](https://doi.org/10.3847/2041-8213/abdf5b)
- González, E., Kremer, K., Fragione, G., et al. 2022, *ApJ*, 940, 131, doi: [10.3847/1538-4357/ac9b0f](https://doi.org/10.3847/1538-4357/ac9b0f)
- Goodwin, S. P., & Whitworth, A. P. 2004, *A&A*, 413, 929, doi: [10.1051/0004-6361:20031529](https://doi.org/10.1051/0004-6361:20031529)
- Greene, J. E., Strader, J., & Ho, L. C. 2020, *ARA&A*, 58, 257, doi: [10.1146/annurev-astro-032620-021835](https://doi.org/10.1146/annurev-astro-032620-021835)
- Grudić, M. Y., Guszejnov, D., Hopkins, P. F., et al. 2018, *MNRAS*, 481, 688, doi: [10.1093/mnras/sty2303](https://doi.org/10.1093/mnras/sty2303)
- Grudić, M. Y., Diederik Kruijssen, J. M., Faucher-Giguère, C.-A., et al. 2021, *Monthly Notices of the Royal Astronomical Society*, 506, 3239, doi: [10.1093/mnras/stab1894](https://doi.org/10.1093/mnras/stab1894)
- Harris, W. E. 1996, *AJ*, 112, 1487, doi: [10.1086/118116](https://doi.org/10.1086/118116)
- Heger, A., & Woosley, S. E. 2002, *The Astrophysical Journal*, 567, 532, doi: [10.1086/338487](https://doi.org/10.1086/338487)
- Heggie, D., & Hut, P. 2003, *The Gravitational Million-Body Problem: A Multidisciplinary Approach to Star Cluster Dynamics*
- Hénon, M. 1961, *Annales d'Astrophysique*, 24, 369
- Hong, J., Askar, A., Giersz, M., Hypki, A., & Yoon, S.-J. 2020, *MNRAS*, 498, 4287, doi: [10.1093/mnras/staa2677](https://doi.org/10.1093/mnras/staa2677)
- Hurley, J. R., Pols, O. R., & Tout, C. A. 2000, *MNRAS*, 315, 543, doi: [10.1046/j.1365-8711.2000.03426.x](https://doi.org/10.1046/j.1365-8711.2000.03426.x)
- Hurley, J. R., Tout, C. A., & Pols, O. R. 2002, *Monthly Notices of the Royal Astronomical Society*, 329, 897, doi: [10.1046/j.1365-8711.2002.05038.x](https://doi.org/10.1046/j.1365-8711.2002.05038.x)
- Karlssohn, T., Bromm, V., & Bland-Hawthorn, J. 2013, *Reviews of Modern Physics*, 85, 809, doi: [10.1103/RevModPhys.85.809](https://doi.org/10.1103/RevModPhys.85.809)
- King, I. R. 1966, *AJ*, 71, 64, doi: [10.1086/109857](https://doi.org/10.1086/109857)
- Kremer, K., Chatterjee, S., Ye, C. S., Rodriguez, C. L., & Rasio, F. A. 2019, *ApJ*, 871, 38, doi: [10.3847/1538-4357/aaf646](https://doi.org/10.3847/1538-4357/aaf646)
- Kremer, K., Ye, C. S., Chatterjee, S., Rodriguez, C. L., & Rasio, F. A. 2018, *The Astrophysical Journal Letters*, 855, L15, doi: [10.3847/2041-8213/aab26c](https://doi.org/10.3847/2041-8213/aab26c)
- Kremer, K., Ye, C. S., Chatterjee, S., Rodriguez, C. L., & Rasio, F. A. 2020a, in *Star Clusters: From the Milky Way to the Early Universe*, ed. A. Bragaglia, M. Davies, A. Sills, & E. Vesperini, Vol. 351, 357–366, doi: [10.1017/S1743921319007269](https://doi.org/10.1017/S1743921319007269)
- Kremer, K., Spera, M., Becker, D., et al. 2020b, *ApJ*, 903, 45, doi: [10.3847/1538-4357/abb945](https://doi.org/10.3847/1538-4357/abb945)
- Kroupa, P. 2001, *Monthly Notices of the Royal Astronomical Society*, 322, 231, doi: [10.1046/j.1365-8711.2001.04022.x](https://doi.org/10.1046/j.1365-8711.2001.04022.x)
- Kruijssen, J. M. D. 2012, *MNRAS*, 426, 3008, doi: [10.1111/j.1365-2966.2012.21923.x](https://doi.org/10.1111/j.1365-2966.2012.21923.x)
- Küpper, A. H. W., Maschberger, T., Kroupa, P., & Baumgardt, H. 2011, *MNRAS*, 417, 2300, doi: [10.1111/j.1365-2966.2011.19412.x](https://doi.org/10.1111/j.1365-2966.2011.19412.x)
- Lamers, H. J. G. L. M., Baumgardt, H., & Gieles, M. 2010, *Monthly Notices of the Royal Astronomical Society*, 409, 305, doi: [10.1111/j.1365-2966.2010.17309.x](https://doi.org/10.1111/j.1365-2966.2010.17309.x)
- Larsen, S. S. 1999, *A&AS*, 139, 393, doi: [10.1051/aas:1999509](https://doi.org/10.1051/aas:1999509)
- Liu, H.-L., Liu, T., Evans, Neal J., I., et al. 2021, *MNRAS*, 505, 2801, doi: [10.1093/mnras/stab1352](https://doi.org/10.1093/mnras/stab1352)
- Loeb, A., & Rasio, F. A. 1994, *ApJ*, 432, 52, doi: [10.1086/174548](https://doi.org/10.1086/174548)
- Mackey, A. D., & Gilmore, G. F. 2003, *MNRAS*, 338, 85, doi: [10.1046/j.1365-8711.2003.06021.x](https://doi.org/10.1046/j.1365-8711.2003.06021.x)
- Madau, P., & Rees, M. J. 2001, *ApJL*, 551, L27, doi: [10.1086/319848](https://doi.org/10.1086/319848)
- McKernan, B., Ford, K. E. S., Lyra, W., & Perets, H. B. 2012, *MNRAS*, 425, 460, doi: [10.1111/j.1365-2966.2012.21486.x](https://doi.org/10.1111/j.1365-2966.2012.21486.x)
- McLaughlin, D. E., & van der Marel, R. P. 2005, *ApJS*, 161, 304, doi: [10.1086/497429](https://doi.org/10.1086/497429)
- Miller, M. C., & Hamilton, D. P. 2002, *MNRAS*, 330, 232, doi: [10.1046/j.1365-8711.2002.05112.x](https://doi.org/10.1046/j.1365-8711.2002.05112.x)

- Morscher, M., Pattabiraman, B., Rodriguez, C., Rasio, F. A., & Umbreit, S. 2015, *ApJ*, 800, 9, doi: [10.1088/0004-637X/800/1/9](https://doi.org/10.1088/0004-637X/800/1/9)
- Pols, O. R., Schröder, K.-P., Hurley, J. R., Tout, C. A., & Eggleton, P. P. 1998, *MNRAS*, 298, 525, doi: [10.1046/j.1365-8711.1998.01658.x](https://doi.org/10.1046/j.1365-8711.1998.01658.x)
- Portegies Zwart, S. F., Baumgardt, H., Hut, P., Makino, J., & McMillan, S. L. W. 2004, *Nature*, 428, 724, doi: [10.1038/nature02448](https://doi.org/10.1038/nature02448)
- Portegies Zwart, S. F., & McMillan, S. L. W. 2002, *ApJ*, 576, 899, doi: [10.1086/341798](https://doi.org/10.1086/341798)
- Portegies Zwart, S. F., McMillan, S. L. W., & Gieles, M. 2010, *ARA&A*, 48, 431, doi: [10.1146/annurev-astro-081309-130834](https://doi.org/10.1146/annurev-astro-081309-130834)
- Purohit, R. A., Fragione, G., Rasio, F. A., Petter, G. C., & Hickox, R. C. 2024, *AJ*, 167, 191, doi: [10.3847/1538-3881/ad3103](https://doi.org/10.3847/1538-3881/ad3103)
- Rizzuto, F. P., Naab, T., Spurzem, R., et al. 2022, *MNRAS*, 512, 884, doi: [10.1093/mnras/stac231](https://doi.org/10.1093/mnras/stac231)
- Rodriguez, C. L., Amaro-Seoane, P., Chatterjee, S., et al. 2018, *PhRvD*, 98, 123005, doi: [10.1103/PhysRevD.98.123005](https://doi.org/10.1103/PhysRevD.98.123005)
- Rodriguez, C. L., Hafen, Z., Grudić, M. Y., et al. 2023, *MNRAS*, 521, 124, doi: [10.1093/mnras/stad578](https://doi.org/10.1093/mnras/stad578)
- Rodriguez, C. L., Zevin, M., Amaro-Seoane, P., et al. 2019, *PhRvD*, 100, 043027, doi: [10.1103/PhysRevD.100.043027](https://doi.org/10.1103/PhysRevD.100.043027)
- Rodriguez, C. L., Weatherford, N. C., Coughlin, S. C., et al. 2022, *ApJS*, 258, 22, doi: [10.3847/1538-4365/ac2edf](https://doi.org/10.3847/1538-4365/ac2edf)
- Rui, N. Z., Kremer, K., Weatherford, N. C., et al. 2021, *ApJ*, 912, 102, doi: [10.3847/1538-4357/abed49](https://doi.org/10.3847/1538-4357/abed49)
- Rydberg, C.-E., Zackrisson, E., Lundqvist, P., & Scott, P. 2013, *MNRAS*, 429, 3658, doi: [10.1093/mnras/sts653](https://doi.org/10.1093/mnras/sts653)
- Ryon, J. E., Bastian, N., Adamo, A., et al. 2015, *MNRAS*, 452, 525, doi: [10.1093/mnras/stv1282](https://doi.org/10.1093/mnras/stv1282)
- Ryon, J. E., Gallagher, J. S., Smith, L. J., et al. 2017, *ApJ*, 841, 92, doi: [10.3847/1538-4357/aa719e](https://doi.org/10.3847/1538-4357/aa719e)
- San Roman, I., Sarajedini, A., Holtzman, J. A., & Garnett, D. R. 2012, *Monthly Notices of the Royal Astronomical Society*, 426, 2427, doi: [10.1111/j.1365-2966.2012.21400.x](https://doi.org/10.1111/j.1365-2966.2012.21400.x)
- Shrivastava, R., & Kremer, K. 2022, *Research Notes of the American Astronomical Society*, 6, 157, doi: [10.3847/2515-5172/ac87b1](https://doi.org/10.3847/2515-5172/ac87b1)
- Spera, M., & Mapelli, M. 2017, *MNRAS*, 470, 4739, doi: [10.1093/mnras/stx1576](https://doi.org/10.1093/mnras/stx1576)
- Spitzer, L. 1987, *Dynamical evolution of globular clusters*
- Szécsi, D., Agrawal, P., Wünsch, R., & Langer, N. 2022, *A&A*, 658, A125, doi: [10.1051/0004-6361/202141536](https://doi.org/10.1051/0004-6361/202141536)
- The LIGO Scientific Collaboration, the Virgo Collaboration, the KAGRA Collaboration, et al. 2021a, *arXiv e-prints*, arXiv:2111.03634, <https://arxiv.org/abs/2111.03634>
- . 2021b, *arXiv e-prints*, arXiv:2111.03606, <https://arxiv.org/abs/2111.03606>
- Umbreit, S., Fregeau, J. M., Chatterjee, S., & Rasio, F. A. 2012, *ApJ*, 750, 31, doi: [10.1088/0004-637X/750/1/31](https://doi.org/10.1088/0004-637X/750/1/31)
- Weatherford, N. C., Kiroğlu, F., Fragione, G., et al. 2023, *ApJ*, 946, 104, doi: [10.3847/1538-4357/acbcc1](https://doi.org/10.3847/1538-4357/acbcc1)
- Wilkinson, M. I., Hurley, J. R., Mackey, A. D., Gilmore, G. F., & Tout, C. A. 2003, *MNRAS*, 343, 1025, doi: [10.1046/j.1365-8711.2003.06749.x](https://doi.org/10.1046/j.1365-8711.2003.06749.x)
- Wilson, C. P. 1975, *AJ*, 80, 175, doi: [10.1086/111729](https://doi.org/10.1086/111729)
- Woosley, S. E. 2017, *ApJ*, 836, 244, doi: [10.3847/1538-4357/836/2/244](https://doi.org/10.3847/1538-4357/836/2/244)
- Woosley, S. E., Blinnikov, S., & Heger, A. 2007, *Nature*, 450, 390, doi: [10.1038/nature06333](https://doi.org/10.1038/nature06333)
- Ye, C. S., Kremer, K., Rodriguez, C. L., et al. 2022, *The Astrophysical Journal*, 931, 84, doi: [10.3847/1538-4357/ac5b0b](https://doi.org/10.3847/1538-4357/ac5b0b)